



Universiteit
Leiden
The Netherlands

Towards a mechanistic understanding of nanoparticle behavior using zebrafish

Arias Alpizar, G.

Citation

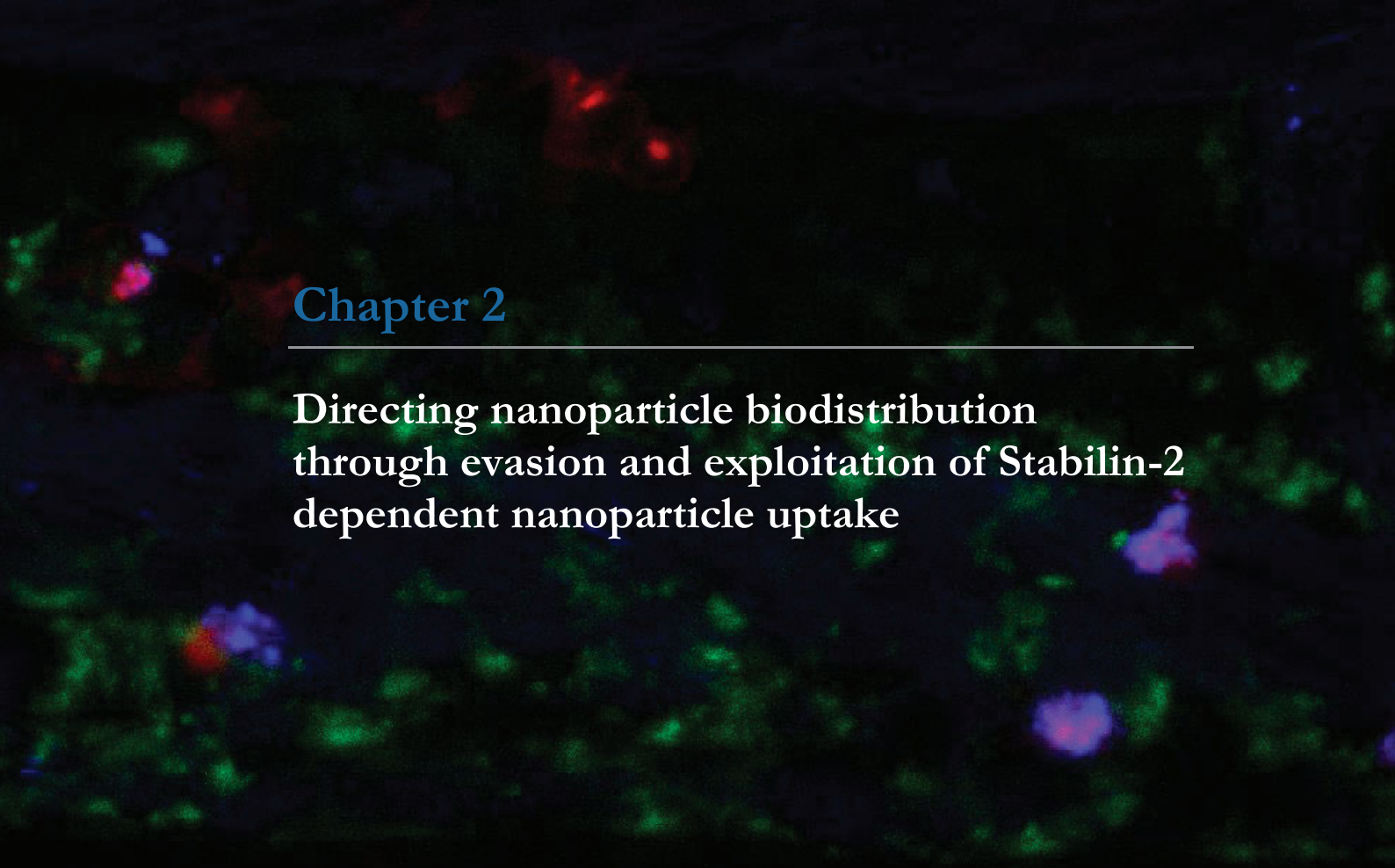
Arias Alpizar, G. (2021, November 4). *Towards a mechanistic understanding of nanoparticle behavior using zebrafish*. Retrieved from <https://hdl.handle.net/1887/3239024>

Version: Publisher's Version

License: [Licence agreement concerning inclusion of doctoral thesis in the Institutional Repository of the University of Leiden](#)

Downloaded from: <https://hdl.handle.net/1887/3239024>

Note: To cite this publication please use the final published version (if applicable).

A fluorescence microscopy image showing a field of cells. The cells exhibit various fluorescent signals: green, red, and blue. The green signal is widespread, while red and blue signals are more localized, appearing as distinct spots or clusters within the cells. The background is dark, making the fluorescent signals stand out.

Chapter 2

Directing nanoparticle biodistribution through evasion and exploitation of Stabilin-2 dependent nanoparticle uptake

Published:

Campbell, F.; Bos, F. L.*; Sieber, S*.; Arias-Alpizar, G*; Koch, B. E.; Huwyler, J.; Kros, A.; Bussmann, J., Directing Nanoparticle Biodistribution through Evasion and Exploitation of Stab2-Dependent Nanoparticle Uptake. ACS Nano 2018, 12 (3), 2138-2150.

These authors contributed equally*

Image: Scavenging endothelial cells containing fluorescent hyaluronic acid and nanoparticles (blue), phagocytosed by macrophages (red).

2.1 Abstract

Up to 99% of systemically administered nanoparticles are cleared through the liver. Within the liver, most nanoparticles are thought to be sequestered by macrophages (Kupffer cells), although significant nanoparticle interactions with other hepatic cells have also been observed. To achieve effective cell-specific targeting of drugs through nanoparticle encapsulation, improved mechanistic understanding of nanoparticle–liver interactions is required. Here, we show the caudal vein of the embryonic zebrafish (*Danio rerio*) can be used as a model for assessing nanoparticle interactions with mammalian liver sinusoidal (or scavenger) endothelial cells (SECs) and macrophages. We observe that anionic nanoparticles are primarily taken up by SECs and identify an essential requirement for the scavenger receptor, Stabilin-2 (*stab2*) in this process. Importantly, nanoparticle–SEC interactions can be blocked by dextran sulphate, a competitive inhibitor of Stabilin-2 and other scavenger receptors. Finally, we exploit nanoparticle–SEC interactions to demonstrate targeted intracellular drug delivery resulting in the selective deletion of a single blood vessel in the zebrafish embryo. Together, we propose Stabilin-2 inhibition or targeting as a general approach for modifying nanoparticle–liver interactions of a wide range of nanomedicines.

2.2 Introduction

Cell-type specific targeting is a common goal in nanoparticle drug delivery. However, the inability to efficiently target subpopulations of cells, beyond the macrophages and monocytes of the mononuclear phagocyte system (MPS), has stymied progress of these technologies into clinical use.¹⁻⁴ Up to 99% of systemically administered nanoparticles, of all shapes, sizes, and chemical compositions are cleared through the liver.⁵ While it is generally accepted that nanoparticles are taken up by liver-resident macrophages (Kupffer cells (KCs)),⁶ the principal cell type of the MPS in the liver, significant nanoparticle interactions with other hepatic cells, including liver sinusoidal endothelial cells (LSECs), hepatocytes, and hepatic B-cells, have also been observed.⁷⁻¹⁰ In these instances however, the cell-specific mechanisms underpinning these interactions have not been elucidated. A detailed understanding of exactly where and how nanoparticles are sequestered and cleared within the liver is crucial for the effective optimization of nanoparticle-mediated drug delivery.

The principle function of the liver is to maintain homeostasis. This includes the removal (“scavenging”) of macromolecular and colloidal waste and pathogens from the blood. Within the liver, scavenging function is primarily associated with the hepatic sinusoids,¹¹ specialized blood vessels connecting the hepatic artery and portal vein (incoming blood flow) with the central vein (outgoing blood flow). In these vessels, scavenging function is facilitated by a >10-fold decrease in blood flow velocity.¹² Hepatic sinusoids are primarily composed of LSECs (~70%) and KCs (~20%).¹³ Together these cells comprise the hepatic reticuloendothelial system (RES), a term originally proposed in the early 20th century by Aschoff¹⁴ to include specialized cells that accumulated vital stains. Since then, the term RES has been largely superseded by the MPS, which in the liver sinusoid includes KCs but not LSECs.

Cells with a scavenging function similar to mammalian LSECs have been identified in all vertebrates examined. However, in teleost fish, sharks, and lampreys these cells have not been found in the liver, but are identified in various other organs.¹⁵ Collectively, these cells are known as scavenger endothelial cells (SECs), a specialized endothelial cell type functionally defined as the major clearance site of endogenous macromolecules such as oxidized low-density lipoprotein (oxLDL) and hyaluronic acid (HA) from the blood.¹¹ Mammalian LSECs have also been implicated in clearance of blood-borne viruses from circulation¹⁶⁻¹⁸ and are important cell-types of both the innate and adaptive immune system.^{19, 20} In LSECs, clearance function is mediated through a

relatively small number of pattern-recognition endocytosis receptors.¹¹ Given the wide variety of macromolecules, colloids, and pathogens sequestered by LSECs, these receptors are clearly promiscuous with respect to potential binding partners. However, what general physicochemical properties direct materials to LSECs, to what extent are individual endocytosis receptors involved, and the significance of these interactions in the clearance of nanoparticles from circulation are not clearly defined.

Here, we show a specific part of the zebrafish embryonic vasculature displays functional homology to the mammalian liver sinusoid and includes macrophages/monocytes and functional SECs. Using this model, we are able to study which general properties of nanoparticles result in their uptake by each of these cell types after intravenous injection. For SECs, we reveal an important molecular mechanism required for nanoparticle clearance, involving the transmembrane receptor Stabilin-2, which can be both inhibited and exploited to guide cell-specific nanoparticle-mediated drug delivery.

2.3 Results

A Zebrafish Model for Liposome Biodistribution

Of the myriad nanoparticles reported as potential drug delivery vectors, liposomes are the most widely investigated and the major class of nanoparticles approved for clinical use.^{21, 22} So far, the ability to predict the fate of liposomes following intravenous injection based on lipid composition alone has been limited. Furthermore, the opacity of mammalian models precludes comprehensive assessment of the dynamic behavior of liposomes *in vivo*. Recent studies have shown that the small and transparent zebrafish embryo allows for the direct observation of circulating nanoparticles, including liposomes, and their interactions with cells.²³⁻²⁶ These studies show key aspects of nanoparticle behavior, including uptake by the MPS, are conserved between zebrafish and mammals. We therefore selected this model to identify the influence of lipid composition on liposome biodistribution and the mechanisms of liposome uptake by cells.

Three liposome formulations, either approved for clinical use or under development (Myocet, EndoTAG-1, and AmBisome),²⁷⁻²⁹ were initially selected for intravenous injection into zebrafish embryos. These formulations were specifically chosen to assess the influence of contrasting nanoparticle surface

charge. Myocet is a neutral liposomal-doxorubicin formulation showing extravasation in tumors.²⁷ EndoTAG-1 is a positively charged liposomal-paclitaxel formulation targeting actively growing tumor blood vessels.²⁹ AmBisome is a negatively charged liposomal-amphotericin B formulation used to treat severe fungal infections.²⁸ Fluorescently labeled liposomes (~100 nm in diameter and without encapsulated drugs) based on the lipid composition of these formulations (**Supplementary Table 1**) were injected intravenously into the duct of Cuvier of zebrafish embryos at 54 h post-fertilization (hpf), a stage at which most organ systems are established. Injected embryos were imaged using confocal microscopy at 1, 8, 24, and 48 h post-injection (hpi) (**Figure 1a**), and confocal micrographs were generated for the entire embryo (whole organism level) as well as from a region caudal to the cloaca (tissue level) (**Figure 1b,d** and **Supplementary Figure 1**). We developed a quantification method to compare levels of circulating liposomes, extravasation, and accumulation in different blood vessel types between formulations (**Figure 1c,e-h** and **Supplementary Figure 2**). At 1 hpi, on a whole organism level, all three liposome were found associated with the blood vasculature and over time, the fluorescence associated with freely circulating liposomes within the lumen of the dorsal aorta, decayed exponentially (**Figure 1b,e**). At the tissue level however, clear differences in liposome biodistribution were observed (**Figure 1d**). Consistent with their behavior in mammals, neutral Myocet liposomes were mostly seen circulating within the blood vessel lumen. At 1 hpi, liposome translocation through the vessel wall (extravasation) was already evident, and between 1 and 8 hpi, co-localization with plasma-exposed macrophages was observed (**Figure 1d,g** and **Supplementary Figure 3**). Increasing the size of Myocet liposomes resulted in enhanced uptake by macrophages, whereas surface PEGylation—a strategy widely employed to limit nanoparticle clearance *in vivo*³⁰—effectively inhibited phagocytotic uptake as described previously (**Supplementary Figure 3**).^{23,26}

For EndoTAG-1 and AmBisome, a large fraction of the injected dose was removed from circulation by 1 hpi and 8 hpi respectively, and these formulations were found associated with the vessel wall (**Figure 1e,h**). Strikingly however, anionic AmBisome liposomes associated only with ECs of a subset of blood vessels, namely the caudal vein (CV), the posterior and common cardinal veins (PCV and CCV), and the primary head sinus (PHS) as well as ECs within the caudal hematopoietic tissue (CHT-ECs) (**Figure 1d,f-h**).³¹ These comprise the majority of venous ECs within the zebrafish embryo at this developmental stage.³² Cationic EndoTAG-1 liposomes at 1 hpi associated with all ECs as expected³³ but at later time points remain associated only with venous ECs. AmBisome,

EndoTAG-1, and Myocet are each composed of various mixtures of (phospho)lipids and cholesterol. In these cases, lipid headgroup chemistries, fatty acid chain saturation and cholesterol content, will together combine to affect the overall physicochemical character of the formulated liposomes and consequently their *in vivo* fate.

To limit potential variation in liposome membrane composition, we next formulated and injected ~100 nm liposomes composed of the individual (phospho)lipids constituting AmBisome, EndoTAG-1, and Myocet (**Supplementary Figure 4** and **Table 1**). We also included liposomes composed of 1,2-dioleoyl-*sn*-glycero-3-phospho-(1'-*rac*-glycerol) (DOPG) and 1,2-dioleoyl-*sn*-glycero-3-phosphocholine (DOPC). In these experiments, injected cationic liposomes (measured zeta potential; >30 mV) initially associated with both arterial and venous ECs of the embryonic fish. All anionic liposomes (<-30 mV) associated with venous ECs alone, and the behavior of neutral liposomes was dependent on lipid fatty acid chain saturation, whereby "fluid" liposome membranes (*e.g.* DOPC), rich in unsaturated lipids, are freely circulating, whereas those composed of 'rigid', saturated lipids (*e.g.* 1,2-distearoyl-*sn*-glycero-3-phosphocholine (DSPC)) associated with venous ECs. Of these, liposomes composed of DSPC and DOPG associated with venous ECs of the CCV, PHS, PCV, CHT, and CV most strongly (**Figure 1i**, and **Supplementary Figure 4a,d**). Both these liposomes also accumulated in macrophages within the CHT and along the CCV (**Supplementary Figure 5**). Differential distribution of nanoparticles over blood vessel networks has previously been attributed to differences in flow patterns.^{9, 25} However, when injections were performed in 4 day-old zebrafish embryos, both DOPG and DSPC liposomes preferentially associated with only a subset of venous ECs along the dorsal side of the PCV (dPCV) (**Figure 1j**). Liposome association with a subset of ECs in a single, straight blood vessel (where flow patterns are expected to be similar throughout) indicated dPCV ECs are a cell type distinct from ventral PCV (vPCV) ECs. Indeed, differentiation of dPCV and vPCV ECs has previously been observed during the induction of lymphatic differentiation and subintestinal vein angiogenesis,^{34, 35} suggesting dPCV differentiation may lead to the expression of specific receptors by these ECs which in turn could mediate the selective binding of DOPG and DSPC liposomes.

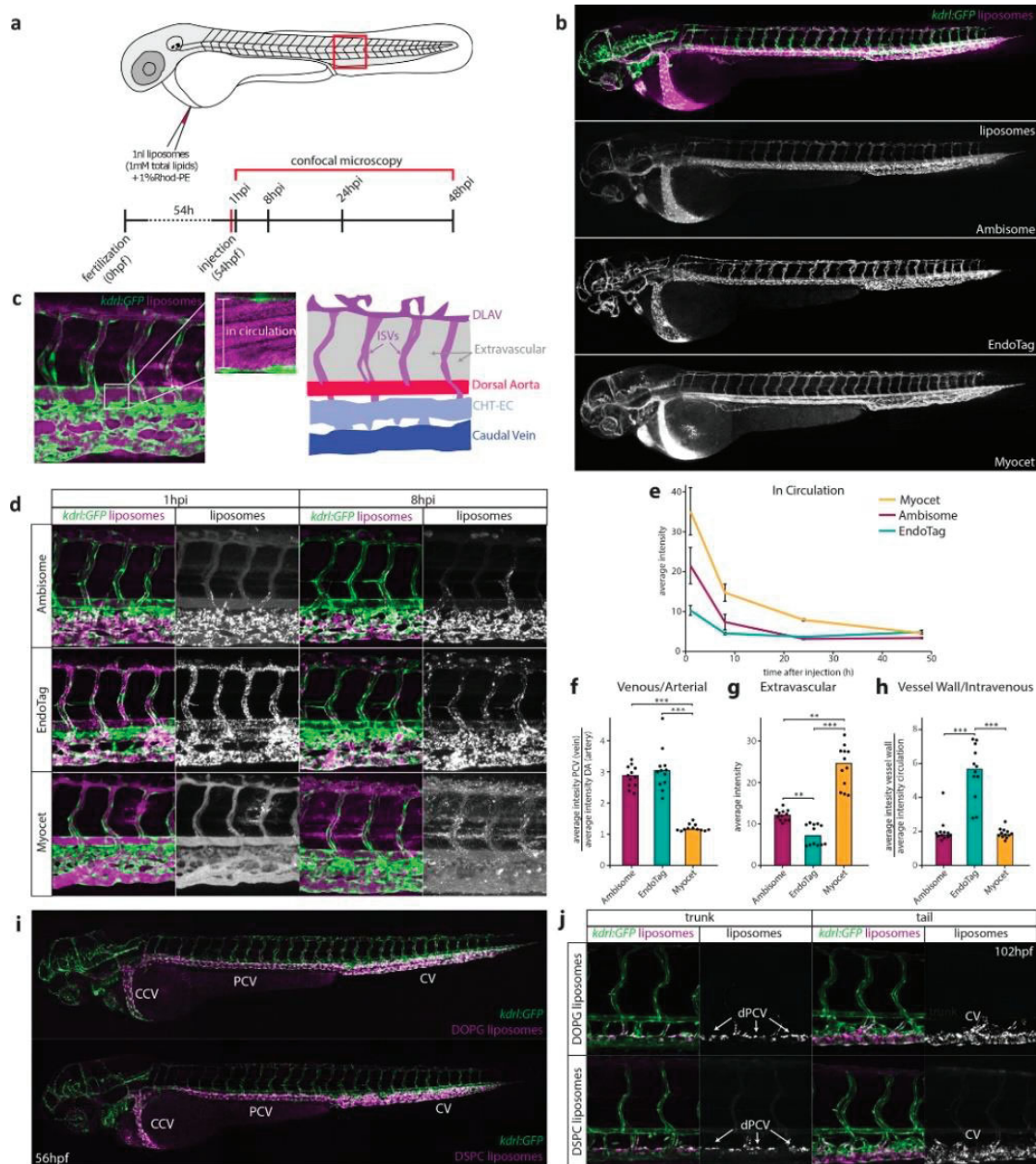


Figure 1. A zebrafish model for liposome biodistribution. (a) Schematic of liposome injection and quantification in zebrafish. Fluorescently labeled liposomes (1 mM total lipids containing 1 mol % Rhod-PE) were injected into the duct of Cuvier at 54 hpf. Confocal microscopy is performed in a defined region (boxed) caudal to the yolk extension at 1, 8, 24, and 48 h after injection. **(b)** Whole-embryo view of liposome distribution in *kdrl:GFP* transgenic embryos, 1 hpi with three different liposome formulations (AmBisome, EndoTAG-1, and Myocet). **(c)** High-resolution imaging allows quantification of liposomes in circulation (measured in the lumen of the dorsal aorta (white box)) and liposome association with different blood vessel types (see Supporting Information). CHT-EC: caudal hematopoietic tissue endothelial cells, DLAV: dorsal longitudinal anastomotic vessel. ISV: intersegmental vessel. **(d)** Tissue level view of liposome distribution in *kdrl:GFP* transgenic embryos, 1 h and 8 h after injection with three different liposome formulations and a single confocal section through the dorsal aorta

(DA) at 1 h after injection. **(e)** Quantification of liposome levels in circulation based on mean rhodamine fluorescence intensity in the lumen of the dorsal aorta at 1, 8, 24, and 48 h after injection (error bars: standard deviation.) n = 6 individually injected embryos per formulation per time point (in two experiments). **(f)** Quantification of liposome levels associated with venous vs. arterial endothelial cells based on rhodamine fluorescence intensity associated with caudal vein (CV) vs. DA at 8 h after injection. **(g)** Quantification of extravascular liposome levels based on rhodamine fluorescence intensity outside of the vasculature between the DLAV and DA at 8 h after injection. **(h)** Quantification of liposome levels associated with the vessel wall based on rhodamine fluorescence intensity associated with all endothelial cells relative to rhodamine fluorescence intensity in circulation at 1h after injection. **(f-h)** Bar height represents median values, dots represent individual data points, brackets indicate significantly different values (*: p < 0.05, **: p < 0.01, ***: p < 0.001) based on Kruskal–Wallis and Dunn’s tests with Bonferroni correction for multiple testing. n=12 individually injected embryos per group (in 2 experiments). **(i)** Whole-embryo view of liposome distribution in *kdrl*:GFP transgenic embryos, 1 h after injection with DOPG and DSPC liposomes. Liposome accumulation for both formulations is observed in the primitive head sinus (PHS), common cardinal vein (CCV), posterior cardinal vein (PCV), and caudal vein (CV). **(j)** Tissue level view of liposome distribution in *kdrl*:GFP transgenic embryos, 1 h after injection with DOPG and DSPC liposomes at 102 hpf. Liposome accumulation is observed in the entire caudal vein (CV), but only on the dorsal side of the PCV (dPCV, arrows).

Identification of a Zebrafish EC Type Homologous to Mammalian LSECs

Selective association of liposomes with most venous ECs has not been observed in adult mammals. However, we hypothesized a more restricted subset of ECs in mammals could be functionally related to venous ECs of the embryonic zebrafish. To test this hypothesis, DOPG liposomes were injected intravenously into Tie2:GFP+ adult mice. In these mice, liposomes were removed from circulation within 1 hpi, and a striking accumulation was observed in the liver (**Figure 2a**). Within the liver, liposomes associated with Tie2:GFP+ sinusoidal ECs and with cells identified as KCs based on cell shape and intravascular localization (**Figure 2b**). No liposome accumulation was observed in hepatocytes or other analyzed organs. This suggested venous ECs and macrophages within the CHT and CV of the embryonic zebrafish were functionally homologous to LSECs and KCs of the mammalian liver and comprise the RES in zebrafish embryos. To confirm this, we injected colloidal lithium carmine (Li-Car), the most prominent vital stain originally used to define the mammalian RES, into zebrafish embryos. Making use of the inherent fluorescence of carminic acid,³⁶ we observed accumulation of this colloid in the same blood vessels (CV, CHT, PCV, and PHS) and subcellular structures within venous ECs and macrophages, in which DOPG and DSPC liposomes also accumulate (**Figure 2c**).

A small number of transmembrane receptors are selectively expressed in mammalian LSECs compared to other blood vascular ECs.¹¹ These include the scavenger receptors *Stabilin-1* and *-2*³⁷ and the mannose receptor *Mrc1*. Analysis of the expression patterns of their orthologs (*stab1*, *stab2* and *mrc1a*) in zebrafish embryos confirmed their restricted expression in venous ECs of the PHS, PCV, CHT, and CV as described previously.^{38, 39} Importantly, expression of these genes becomes enriched in the dPCV, matching observed EC binding specificities of both DOPG and DSPC liposomes (**Supplementary Figure 6**). LSECs mediate the scavenging of macromolecular waste including oxLDL and HA through receptor-mediated endocytosis.⁴⁰ Therefore, we injected fluorescently labeled oxLDL and HA (fluoHA) and observed their rapid endocytosis, within the same subset of venous ECs (within the PHS, CCV, (d)PCV, and CV) (**Figure 2d,f**). Based on the conserved uptake of DOPG liposome, oxLDL, fluoHA, and Li-Car from circulation and expression of known LSEC markers by this venous EC subset in zebrafish embryos, we define them as SECs - homologous to mammalian LSECs. In contrast to DSPC and DOPG liposomes and to oxLDL, fluoHA uptake was specific to SECs, and no uptake was observed in macrophages (**Figure 2g**).

We next used fluoHA as a marker for endocytosis in SECs. Co-injection of fluoHA with DSPC or DOPG liposomes resulted in precise intracellular co-localization in all SECs of the embryonic fish, while in macrophages only liposome internalization was observed (**Figure 2h**, and **Supplementary Figure 7**). Intracellular co-localization in LSECs (but not KCs) of fluoHA and DOPG liposomes was conserved in the adult mouse liver (**Figure 2i**). These results demonstrated fluoHA endocytosis is a selective vital marker for SECs in vertebrates and offered a convenient method to study SEC differentiation in the developing zebrafish embryo (**Supplementary Figure 8**). Importantly, we found SECs were present at the earliest time point at which intravenous injection is possible (28 hpf). During embryonic and larval stages, SECs were maintained within the CV, but starting at 52 hpf became gradually restricted to the dPCV. No fluoHA uptake was observed in embryonic veins that develop during later stages, such as in the brain and subintestinal vasculature. These results show that SECs are one of the first EC subtypes to emerge during embryonic development and provide the first analysis of early embryonic SEC differentiation in any vertebrate.

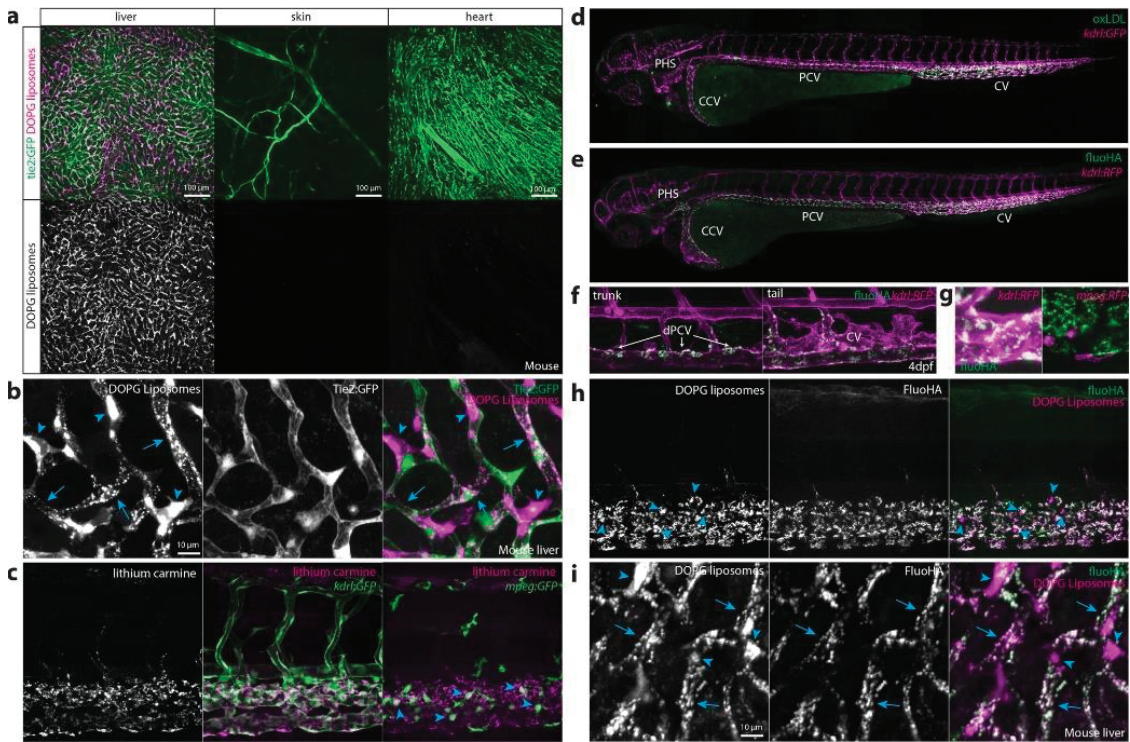


Figure 2. Identification of scavenger endothelial cells (SECs) in zebrafish embryos. (a, b) *Ex vivo* imaging of adult *Tie2:GFP* transgenic mouse organs, 1 h after injection with DOPG liposomes. (a) Liposome accumulation is observed in liver, but not in the ear skin or heart muscle. (b) Within the liver, DOPG liposomes are observed as punctae within *Tie2:GFP*+ sinusoidal ECs (arrows) as well as sinusoid-associated cells which based on shape and position were identified as KCs (arrowheads). (c) Tissue level view of lithium carmine distribution in *kdrl:GFP* and *mpeg:GFP* transgenic zebrafish embryos, 1 h after injection. Lithium carmine (carminic acid) fluorescence co-localizes both with *kdrl:GFP*+ endothelial cells in the caudal vein and *mpeg:GFP*+ monocytes/macrophages (arrowheads) within the CHT. (d) Whole-embryo view of fluorescent oxLDL distribution in *kdrl:GFP* transgenic embryos, 1 h after injection. Accumulation of oxLDL is observed in the PHS, CCV, PCV, and CV. (e) Whole-embryo view of fluoHA distribution in *kdrl:RFP* transgenic embryos, 1 h after injection. Accumulation of fluoHA is observed in the PHS, CCV, PCV, and CV. (f) Tissue level view of fluoHA distribution in *kdrl:RFP* transgenic embryos, 1 h after injection at 102 hpf. FluoHA accumulation is observed in the entire caudal vein (CV), but only on the dorsal side of the PCV (dPCV, arrows). (g) Tissue level view of fluoHA in *kdrl:RFP* and *mpeg:RFP* transgenic embryos. Co-localization of RFP expression and fluoHA is observed only within *kdrl:RFP* endothelial cells, but not *mpeg:RFP* monocytes/macrophages. (h) Tissue level view of co-injected fluoHA and DOPG liposomes, 1 h after injection reveals co-localization in SECs. Monocytes/macrophages (arrowheads) take up DOPG but not fluoHA. (i) *Ex vivo* imaging of adult mouse liver, 1 h after injection with fluoHA and DOPG liposomes reveals widespread co-localization within sinusoidal ECs (arrows). KCs (arrowheads) take up DOPG liposomes only.

Stabilin-2 Is Required for Uptake of Liposomes and Other Nanoparticles by SECs

The precise intracellular co-localization of fluoHA with DOPG and DSPC liposomes in SECs indicated the use of a shared receptor for endocytosis. Importantly, one of the markers for SECs in zebrafish embryos and adult mammals, Stabilin-2, has been identified as the main HA clearance receptor in the mouse liver.⁴⁰ *In vitro*, Stabilin-2 and its paralog Stabilin-1 have been shown to bind to a large variety of endogenous (mostly anionic) macromolecules⁴¹ as well as phosphothiorate-modified antisense oligonucleotides (PS-ASO),⁴² apoptotic cell bodies,⁴³ biotinylated albumin,⁴⁴ and carbon nanotubes.⁴⁵ *In vivo*, Stabilin-1 and Stabilin-2 were shown to mediate sequestration (but not uptake) by LSECs of aged erythrocytes in a phosphatidylserine-dependent manner.⁴⁶ Stabilin-1 and Stabilin-2 are both nonessential genes for development and normal physiology in mice, with mice lacking both Stabilin-1 and Stabilin-2 displaying deficient removal of nephrotoxic macromolecules from circulation.³⁷

To test if stabilins were involved in liposome uptake by SECs, embryos were first pretreated with dextran sulfate - a competitive inhibitor of scavenger receptors, including *stab1* and *stab2*.^{47, 48} Subsequent liposome injection (or co-injection) resulted in a striking loss of liposome uptake by SECs, offset by an increase in circulating liposomes, and particularly in the case of DOPG liposomes, an increase in macrophage uptake (**Figure 3a,b**). In contrast, injection of mannan, a competitive inhibitor of *mrc1a*,⁴⁹ did not inhibit liposome uptake by SECs (data not shown). To identify the specific role of *stab1* and *stab2* in liposome uptake, mutants for both genes were generated through CRISPR/Cas9-mediated mutagenesis. Here, we report the analysis of a *stab2* mutant line, in which we identified a 4nt deletion (*stab2^{ibl2}*), leading to a frameshift in the *stab2* coding sequence and a premature stop codon (C233X) (**Figure 3c** and **Supplementary Figure 9**). This mutation is predicted to remove most conserved *stab2* domains including all fascilin domains, the HA binding Link domain, and the transmembrane and cytoplasmic segments. Homozygous *stab2^{ibl2}* mutants displayed a strong reduction of *stab2*, but not of *stab1* or *mrc1a*, mRNA expression indicating normal SEC differentiation and nonsense-mediated decay of *stab2^{ibl2}* mRNA (**Supplementary Figure 10**). *Stab2^{ibl2}* mutants survived throughout embryonic development without defects in either blood or lymphatic vascular systems, which were described previously for *stab2* morphants,^{50, 51} and fertile adults were identified in normal Mendelian ratios (**Figure 3d,e**). Consistent with the increase in circulating HA levels observed in mouse *Stab2* knockouts,⁵² a complete loss of fluoHA uptake by SECs was observed in zebrafish

stab2^{ibl2} mutants, showing a conserved role for *stab2* in HA clearance in vertebrates (**Figure 3f**). Importantly, when either DOPG or DSPC liposomes were injected in *stab2^{ibl2}* mutants, a strong reduction of liposome endocytosis by SECs was observed, offset by an increase in circulating liposome levels and an increase in macrophage uptake (**Figure 3g,h**). Differential liposome uptake in neighboring venous ECs of embryos with a mosaic loss of *stab2* function indicated a cell-autonomous role of *stab2* function in liposome uptake by SECs (**Supplementary Figure 11**). For the original three liposome formulations screened, loss of *stab2* function affected AmBisome, but not Myocet or EndoTAG-1 biodistribution (**Figure 3i,k**). Since both AmBisome and EndoTAG-1 accumulated within SECs of wild-type embryos, *stab2*-mediated uptake by SECs appears dependent on specific physicochemical properties of liposomes and *stab2* does not function in the clearance of cationic liposomes.

In vivo, several other scavenger receptors with similar binding profiles to *stab2* are expressed,¹¹ not only on SECs but also on other endothelial cells and macrophages. Given the significant increase in circulating DOPG, DSPC, and AmBisome liposomes in *stab2^{ibl2}* mutants, *stab2* clearly plays a dominant role in removal of these liposomes from circulation compared to other scavenger receptors (including the structurally related *stab1*). Similarly, clearance of PS-ASOs was recently shown to be dominated by Stab2 in the mouse liver.⁴² To test the generality of *stab2* function, several other polyanionic nanoparticles were injected in wild-type and *stab2^{ibl2}* mutant embryos as well as following dextran sulfate injection (**Figure 4a-l**). These included endogenous (DOPS liposomes, a model for apoptotic cell fragments), viral (Cowpea Chlorotic Mottle Virus-like particles, CCMV VLPs),⁵³ polymeric (polymersomes⁵⁴ and polystyrene beads), and inorganic (quantum dots, QDs) nanoparticles. All of these particles were endocytosed selectively by SECs in zebrafish embryos, and in all cases SEC endocytosis could be inhibited by dextran sulfate. However, not all nanoparticles were dependent on *stab2* for SEC endocytosis.

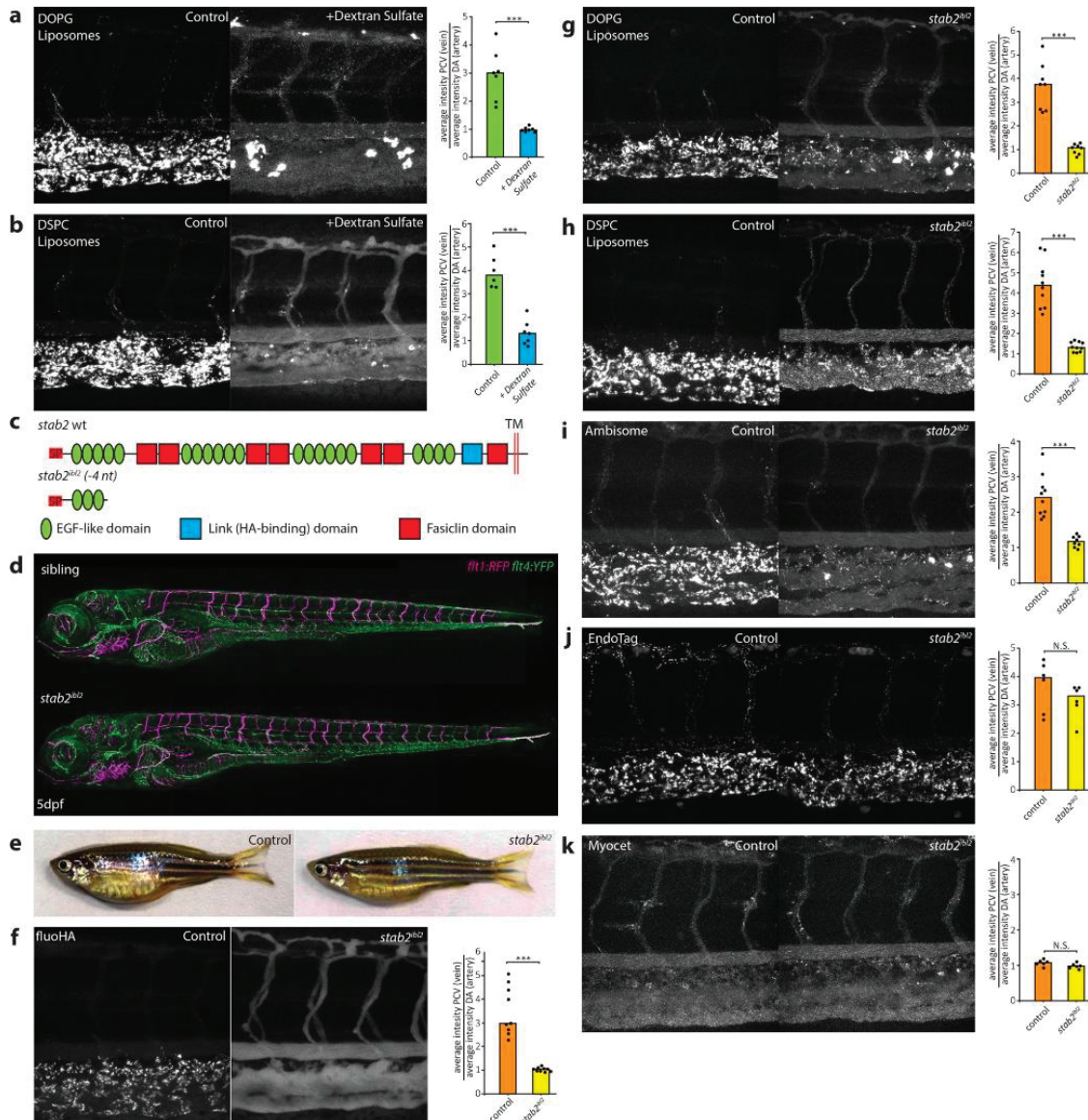


Figure 3. Stabilin-2 is required for anionic liposome uptake by SECs. (a, b) Tissue level view of DOPG and DSPC liposome distribution at 1 hpi in control and dextran sulfate injected embryos, with quantification of liposome levels associated with venous vs. arterial endothelial cells (ECs) based on rhodamine fluorescence intensity associated with CV vs. DA. (c) *stab2* domain structure predicted to be expressed from the wild-type *stab2* and the *stab2^{ibl2}* allele. (d) Whole-embryo view of *flt1:RFP*, *flt4:YFP* double transgenic embryos at 5 dpf to visualize blood vascular and lymphatic development. No defects were identified during (lymph)angiogenesis and vascular patterning in *stab2^{ibl2}* homozygous embryos compared to sibling controls. (e) Fertile adult females (*stab2^{ibl2}* homozygous and sibling controls) at 3 months post-fertilization. Tissue level view of fluoHA (f) DOPG (g), DSPC (h), AmBisome (i), EndoTAG-1 (j), and Myocet (k) liposome distribution at 1 hpi in *stab2^{ibl2}* and sibling control embryos, with quantification of liposome levels associated with venous vs. arterial ECs based on rhodamine fluorescence intensity associated with CV vs. DA. (a, b, f–k) Bar height represents median values, dots represent individual data points, and brackets indicate significantly different values (*: $p < 0.05$, **: $p < 0.01$, ***: $p < 0.001$, N.S.: not significant) based on Mann–Whitney test. $n = 6-10$.

Although uptake by SECs of DOPS liposomes, polymersomes, and polystyrene nanoparticles was strongly decreased in *stab2^{ibl2}* mutants, uptake of CCMV VLPs was only partly dependent on Stabilin-2 and QD uptake appeared *stab2*-independent. Alternatively, QD uptake by SECs is also mediated in part by *stab2*, but its function is masked in *stab2^{ibl2}* mutants through redundancy with other scavenger receptors (such as *stab1*) that can be inhibited by dextran sulfate. CCMV VLPs (28 nm) and QDs (<10 nm) were the smallest nanoparticles screened in this study, suggesting size may be an important determinant of scavenger receptor–nanoparticle interactions.

Targeted Liposomal Drug Delivery to SECs

Finally, to demonstrate we could extend the observed interaction of nanoparticles with SECs to cell-selective drug delivery, we encapsulated a model drug, clodronic acid, within DSPC liposomes (**Supplementary Table S2**). Clodronic acid requires active transport (endocytosis or phagocytosis) across the target cell membrane to illicit a cytotoxic effect.⁵⁵ Liposome-mediated intracellular delivery of clodronic acid into monocytes/macrophages is used extensively as a research tool to selectively remove these cell populations *in vivo*.⁵⁶ After 12–24 hpi, synchronous changes in the morphology of the CHT and caudal vein ECs were observed, followed by a gradual loss of *kdrl*:GFP endothelial cells or cell fragments and ultimately leading to the complete disappearance of the caudal vein between 24 and 48 hpi (**Figure 5a-d**). The PCV and other cell types within the CHT, including *mpeg*:GFP macrophages (most of which are not exposed to circulating nanoparticles) as well as *mpx*:GFP neutrophils, were largely unaffected (**Supplementary Figure 12**). Injection of free clodronic acid (a control demonstrating the requirement of liposomal encapsulation) did not result in any observable changes to the venous endothelium. Similarly, injection of freely circulating DOPC-clodronic acid liposomes (a control demonstrating the requirement of selective nanoparticle uptake by SECs) did not affect the venous endothelium. The development of the dorsal aorta was unaffected by deletion of the CV and CHT, and blood supply to the caudal parts of the embryo was maintained through a rerouting of blood cells into the intersegmental vessels and dorsal longitudinal anastomotic vessel (DLAV). Embryos with a complete loss of the CV and CHT endothelial cells were agile and could survive at least until 6 dpf. Imaging of fluorescent DSPC-clodronic acid liposomes revealed selective *stab2*-dependent uptake by SECs analogous to empty DSPC liposomes (**Figure 5e**). Importantly, loss of *stab2* function as observed in *stab2^{ibl2}* mutant embryos

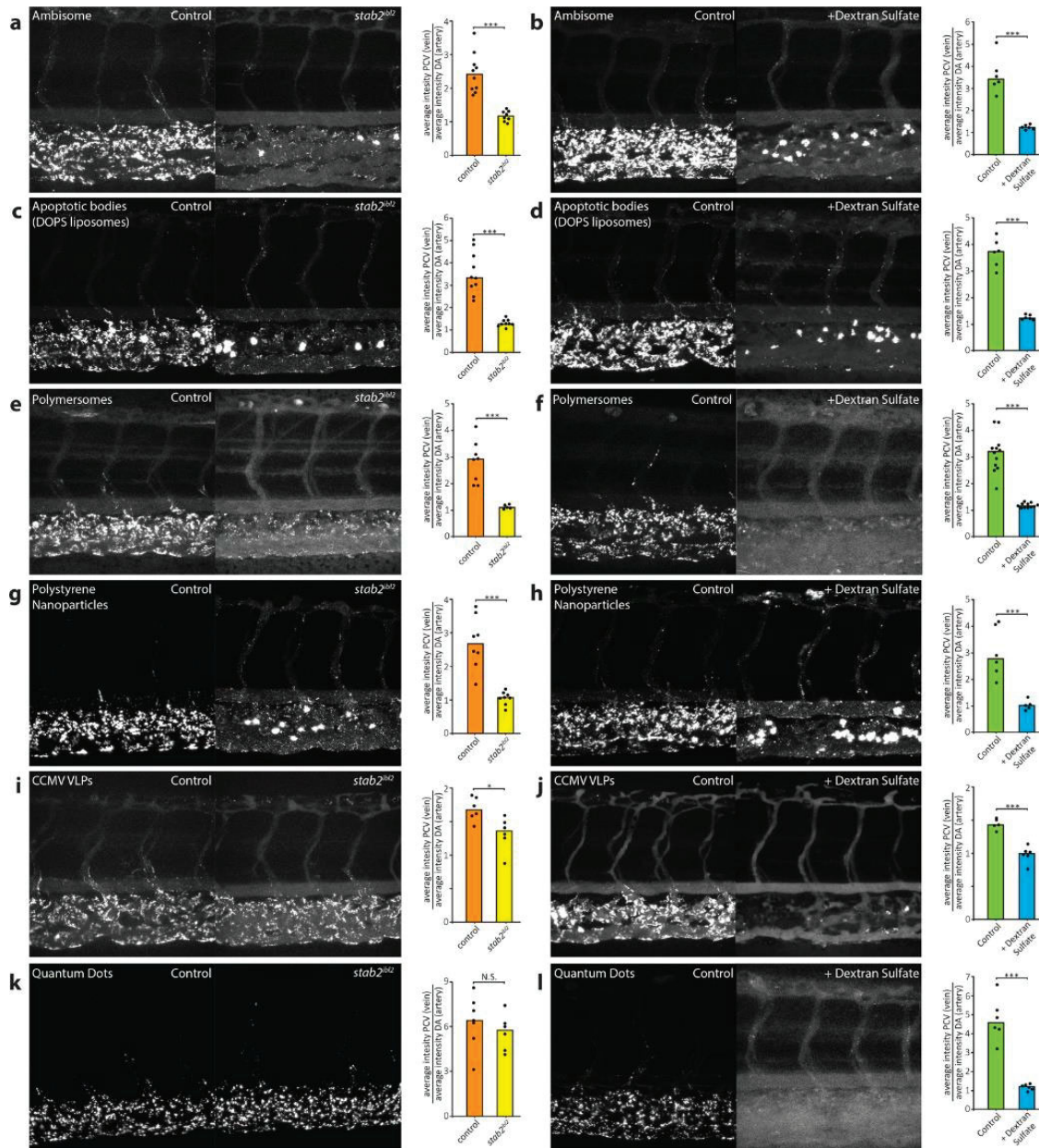


Figure 4. *stab2*-mediated scavenging of anionic nanoparticles *in vivo*. (a–i) Tissue level view of DOPS liposome (a, b), PIB-PEG polymersome (c, d), carboxylated polystyrene nanoparticle (e, f), CCMV virus-like particle (g, h), and carboxylated quantum dot (i, j) distribution at 1 hpi in *stab2^{ib/ib2}* and sibling control embryos (a, c, e, g, i) or control and dextran sulfate injected embryos (b, d, f, h, j). Quantification of nanoparticle levels associated with venous vs arterial endothelial cells based on rhodamine fluorescence intensity associated with caudal vein vs DA. (a–j) Bar height represents median values, dots represent individual data points, and brackets indicate significantly different values (*: $p < 0.05$, **: $p < 0.01$, ***: $p < 0.001$, N.S.: not significant) based on Mann–Whitney test. $n = 5–12$ per group (in two experiments).

rescued the CV phenotype induced by injection of DSPC-clodronic acid liposomes (**Figure 5f-h**). These results identify Stabilin-2-mediated uptake of liposomes by SECs as a simple strategy for intracellular compound delivery to this cell type in zebrafish embryos.

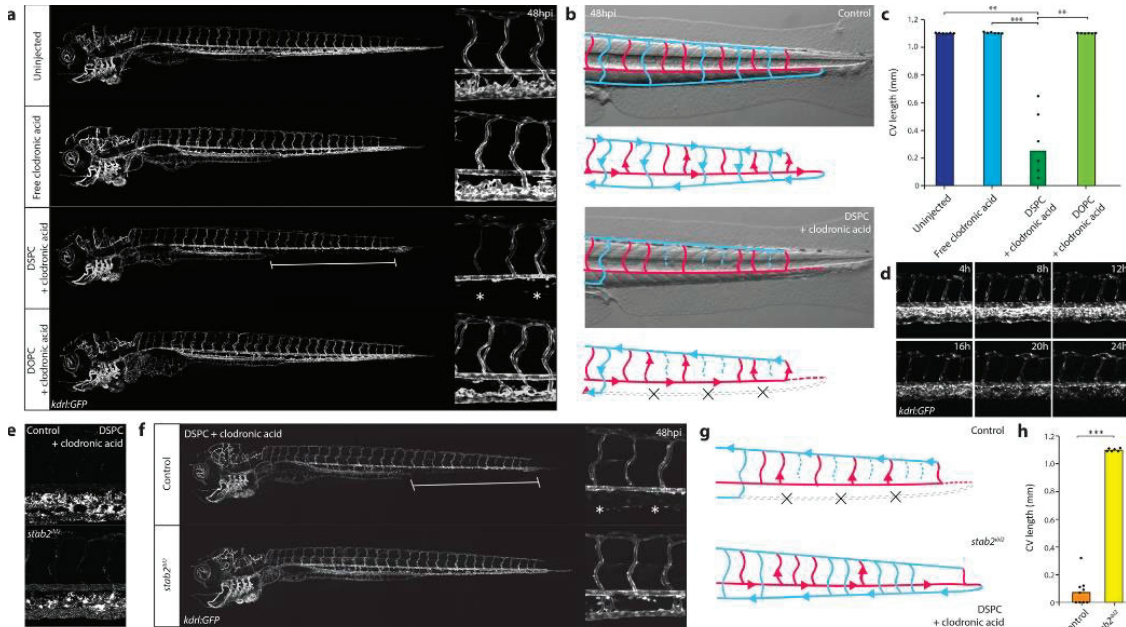


Figure 5. Nanoparticle-mediated SEC deletion. **(a)** Whole-embryo and tissue level views at 48 hpi of the blood vasculature in *kdrl:GFP* transgenic control embryos, embryos injected with 1 mg/mL clodronic acid, or embryos injected with liposomes containing 1 mg/mL clodronic acid (DSPC or DOPC liposomes). Complete deletion of the caudal vein is observed in embryos injected with DSPC liposomes containing clodronic acid (brackets and asterisks). **(b)** Schematic representation of blood flow in control embryos or embryos injected with DSPC liposomes containing 1 mg/mL clodronic acid. Blue indicates venous or capillary blood vessels, and red indicates arterial blood vessels. Arrowheads indicate direction of blood flow. The removal of the CV (dashed lines) leads to a rerouting of blood flow through the DLAV. **(c)** Quantification of PCV length in injected embryos. Bar height represents median values, dots represent individual data points, and brackets indicate significant values (**: $p < 0.01$, ***: $p < 0.001$) based on Kruskal-Wallis and Dunn's tests with Bonferroni correction for multiple testing. $n = 6$ individually injected embryos per group (in two experiments). **(d)** Progression of SEC deletion. Individual frames from Movie S2 in <https://pubs.acs.org/doi/abs/10.1021/acsnano.7b06995>, at indicated time points after injection of DSPC liposomes containing 1 mg/mL clodronic acid, injected into *kdrl:GFP* transgenic embryos. SEC fragmentation in this case is observed mostly between 12 hpi and 16 hpi, followed by a gradual loss of fluorescence or removal of cellular debris. **(e)** Tissue level view of distribution of DSPC liposomes containing 1 mg/mL clodronic acid at 1 hpi in *stab2^{ibl2}* and sibling control embryos. **(f)** Whole-embryo and tissue level views at 48 hpi of the blood vasculature in *kdrl:GFP* transgenic *stab2^{ibl2}* and sibling embryos. Embryos were injected with DSPC liposomes containing 1 mg/mL clodronic acid. Complete deletion of the caudal vein is observed in sibling control (brackets and asterisks), but not *stab2^{ibl2}* mutant embryos. **(g)** Schematic representation of blood flow in sibling control embryos or *stab2^{ibl2}* homozygous mutants, both injected with DSPC liposomes containing 1 mg/mL clodronic acid. **(h)** Quantification of PCV length in injected embryos. Bar height represents median values, dots represent individual data points, and brackets indicate significant values (***: $p < 0.001$) based on Kruskal-Wallis and Dunn's tests with Bonferroni correction for multiple testing. $n = 6$ individually injected embryos per group (in two experiments).

liposomes containing approximately 1 mg/mL clodronic acid. Blue indicates venous or capillary blood vessels, and red indicates arterial blood vessels. Arrowheads indicate direction of blood flow (based on observations from Movie S3, that can be found in <https://pubs.acs.org/doi/abs/10.1021/acsnano.7b06995>). The removal of the CV (dashed lines) leads to a rerouting of blood flow through the DLAV in control embryos but not in *stab2^{ibl2}* homozygous mutants. **(h)** Quantification of PCV length in injected embryos. Bar height represents median values, dots represent individual data points, and brackets indicate significant values (***: $p < 0.001$) based on Mann–Whitney test.

2.4 Discussion and Conclusion

We show Stabilin-2 is an important (scavenger) receptor mediating the uptake of circulating nanoparticles by SECs. In particular, anionic nanoparticles, between 50 and 250 nm in size, are avidly taken up by SECs in a *stab2*-dependent fashion. Here, binding and uptake appear independent of material and functional properties of nanoparticles and are solely dependent on surface charge. Given the comparable sizes and surface charge of many blood-borne viruses,^{16-18, 57} clearance of these circulating pathogens by LSECs is also potentially mediated by *stab2*. These findings, combined with the high expression of *stab2* by LSECs within the mammalian liver,¹¹ implicate SECs as an important cell-type in the binding, uptake, and clearance of administered nanoparticles. As such, we support the re-adoption of the RES, over the MPS, as the most accurate term to describe the specialized cellular components involved in nanoparticle clearance from circulation.⁵⁸

The ultimate goal of many nanoparticle-based technologies is cell-type-specific targeting. Yet reported targeting efficiencies rarely surpass 1% of the total injected nanoparticle dose.⁴ A major contributing factor has been off-target nanoparticle interactions within the mammalian liver.⁵ By revealing the molecular basis of nanoparticle interactions with specific cells of the embryonic zebrafish, we have been able to demonstrate nanoparticle targeting of, and drug delivery to, specific cell types with homologues in the mammalian liver. In addition, we show these interactions can be effectively inhibited by dextran sulfate. As *stab2* is not essential for normal adult physiology,³⁷ this offers a simple method to extend circulation lifetimes of nanoparticles by minimizing potential off-target liver interactions.⁵⁹ This will likely be particularly beneficial in instances where active targeting of nanoparticles to cell types beyond the liver (*e.g.* cancer cells) is desired.

Importantly, the SEC/selective drug delivery we describe has not resulted from adding further complexity to nanoparticle designs. Instead, through systematic

screening of “simple” nanoparticles (*i.e.* liposomes composed of a single phospholipid), we have established what general properties and molecular mechanisms direct nanoparticles to specific cell types. The use of the embryonic zebrafish as a model organism, and the ability to visualize nanoparticle–cell interactions at high resolution in living organisms, has been essential in this process. We therefore propose that the embryonic zebrafish, with its established extensive genetic toolkit, is a valuable preclinical *in vivo* model allowing screening, optimization, and mechanistic understanding of nanoparticle biodistribution, predictive of their behavior in mammals.²⁶

2.5 Materials and Methods

Reagents

Fluorescein-labeled hyaluronic acid (fluoHA) was prepared through conjugation of hyaluronic acid (100 kDa) with fluorescein isothiocyanate (Isomer I, Sigma-Aldrich) as previously described.⁶⁰ Additional fluoHA was provided as a kind gift from W. Jiskoot (Leiden University, The Netherlands). Colloidal Li-Car was prepared as previously described.⁶¹ Rhodamine-loaded polymersomes on polyisobutadiene/ polyethylene glycol (PIB/PEG) block copolymers⁵⁴ were a kind gift from S. Askes and S. Bonnet (Leiden University, The Netherlands). Atto-647 labeled CCMV-virus-like particles ($t = 3$, 28 nm)⁵³ were a kind gift from M. de Ruiter and J. Cornelissen (Twente University, The Netherlands). Purchased reagents are described in the Supporting Information.

Liposome Preparation and Characterization

All liposomes (without encapsulated drugs) were formulated in ddH₂O at a total lipid concentration of 1 mM. Individual lipids, as stock solutions (1–10 mM) in chloroform, were combined at the desired molar ratios and dried to a film, first under a stream of N₂ and then >1h under vacuum. With the exception of Myocet 325 and 464 nm, lipid films were hydrated in 1 mL ddH₂O at >65 °C (with gentle vortexing if necessary) to form large/giant multilamellar vesicles. Large unilamellar vesicles were formed through extrusion above the T_m of all lipids (>65 °C, Mini-extruder with heating block, Avanti Polar Lipids, Alabaster, US). Hydrated lipids were passed 11 times through 2 × 400 nm polycarbonate (PC) membranes (Nucleopore Track-Etch membranes, Whatman), followed by 11 times through 2 × 100 nm PC pores. All liposomes were stored at 4 °C. With the exception of DSPC liposomes (significant aggregation after 1 week storage), all

liposomes were stable for at least 1 month. Myocet 325 and 464 nm liposomes were formulated by gentle hydration of lipid films at 35 °C (without vortexing). In the case of 464 nm Myocet liposomes, hydrated lipids were passed through a 800 nm PC membrane 7 times at 35 °C. In the case of 325 nm Myocet liposomes, hydrated lipids were passed through a 400 nm PC membrane 7 times at 35 °C. See **Supporting Information** for nanoparticle characterization methods and **Supplementary Table 1** for all lipid compositions, size, and zeta potentials of nanoparticles used in this study.

Clodronic Acid Encapsulation and Quantification

Lipid films (10 mM total lipids) were hydrated with ddH₂O containing 200 mg/mL⁻¹ clodronic acid (1 mL) and formulated through extrusion as described for the corresponding “empty” liposomes. Unencapsulated clodronic acid was removed by size exclusion chromatography (illustra NAP Sephadex G-25 DNA grade premade columns (GE Healthcare) used according to the supplier’s instructions). Eluted clodronic acid-encapsulated liposomes were diluted 2.5× during SEC and injected without further dilution. Quantification of encapsulated clodronic acid was determined by UV absorbance as previously reported.⁶² Briefly, liposomes were first destroyed through a 1:1 dilution with 1% v/v Triton X-100 solution before further dilution into an acidic CuSO₄ solution (1:2.25:2.25; Liposome-Triton X-100 mix: 3 mM HNO₃: 4 mM CuSO₄). The concentration of clodronic acid was determined by UV absorbance (Cary 3 Bio UV-vis spectrometer) at 240 nm and quantified against a predetermined calibration curve (50 μM to 2.5 mM clodronic acid). All UV-vis absorbance measurements were taken at room temperature. Blanks were made using liposome solutions without encapsulated clodronic acid but prepared otherwise identically (including SEC procedure). The final encapsulated clodronic acid concentration varied between 0.9 and 1.7 mg mL⁻¹ (see **Supplementary Table 2**).

Zebrafish Strains, in Situ Hybridization, and CRISPR/Cas9 Mutagenesis

Zebrafish (*Danio rerio*, strain AB/TL) were maintained and handled according to the guidelines from the Zebrafish Model Organism Database (<http://zfin.org>) and in compliance with the directives of the local animal welfare committee of Leiden University. Fertilization was performed by natural spawning at the beginning of the light period, and eggs were raised at 28.5 °C in egg water (60 ug/mL Instant Ocean sea salts). The following previously established zebrafish lines were used Tg(*kdr1*:GFP)^{s843,63} Tg(*kdr1*:RFP-CAAX)^{s916,38} Tg(*mpeg*:GFP)^{gl22,64} Tg(*mpeg*:RFP-CAAX)^{ump2,65} Tg(*flt1*^{enh}:RFP)^{hu5333,66} Tg(*flt4*^{BAC}:YFP)^{hu7135,67} and

Tg(*mpx:GFP*)^{*uwm1*}.⁶⁸ Whole-mount *in situ* hybridization was performed as described.⁶⁹ Supplementary Table 3 lists primers for probe generation. Cloning-free sgRNAs for CRISPR/Cas9 mutagenesis were designed and synthesized as described.⁷⁰ sgRNAs (125 pg) and cas9 mRNA (300 pg) were co-injected into single-cell wild-type, albino or *flt4:YFP; flt1:RFP* transgenic embryos. Mutagenesis efficacy, founder identification, and genotyping were performed using CRISPR-STAT.⁷¹ The nucleotide sequences and predicted *stab2* amino acid sequences in the *stab2*^{*ibl2*} line are shown in **Supplementary Figure 11** and **Table 3** for guide RNA sequences and genotyping primers. For mosaic analysis, heterozygous embryos (*stab2*^{*ibl/+*}) obtained from a cross between a *stab2*^{*ibl2*} homozygous parent and a *kdrl:GFP* (*stab2*^{*+/+*}) parent were co-injected with sgRNAs (125 pg) and cas9 mRNA (300 pg) to create second-hit mutations in the wildtype allele.

Zebrafish Intravenous Injections

Liposomal formulations were injected into 2 day old zebrafish embryos (52–56 hpf) using a modified microangiography protocol.⁷² Embryos were anesthetized in 0.01% tricaine and embedded in 0.4% agarose containing tricaine before injection. To improve reproducibility of microangiography experiments, 1 nl volumes were calibrated and injected into the sinus venosus/duct of Cuvier. We created a small injection space by penetrating the skin with the injection needle and gently pulling the needle back, thereby creating a small pyramidal space in which the liposomes and polymers were injected. Successfully injected embryos were identified through the backward translocation of venous erythrocytes and the absence of damage to the yolk ball, which would reduce the amount of liposomes in circulation. For injections at later stages (>80 hpf), 0.5 nL volumes were injected into the CCV. The following concentrations were injected: dextran sulfate (20 mg/mL), FluoHA (0.2 mg/mL), oxLDL (1 mg/mL), CCMV-VLP (1 mg/mL), QDs (1:25 dilution), lithium carmine (1:50 dilution), polymersomes (1 mg/mL), latex beads (1:10 dilution). Dextran sulfate was injected 20 min prior to nanoparticle injection.

Zebrafish Imaging and Quantification

For each treatment or time point, at least six individual embryos (biological replicates) using at minimum two independently formulated liposome preparations were imaged using confocal microscopy. Embryos were randomly picked from a dish of 20–60 successfully injected embryos (exclusion criteria were: no backward translocation of erythrocytes after injection and/or damage

to the yolk ball). Confocal z-stacks were captured on a Leica TCS SPE confocal microscope, using a 10× air objective (HCX PL FLUOTAR) or a 40× water-immersion objective (HCX APO L). For whole-embryo views, 3–5 overlapping z-stacks were captured to cover the complete embryo. Laser intensity, gain, and offset settings were identical between stacks and sessions. Images were processed and quantified using the Fiji distribution of ImageJ.^{73,74} Quantification (not blinded) of liposome biodistribution was performed on 40× confocal z-stacks (with an optical thickness of 2 μm/slice) as described in the **Supporting Information**.

Mouse Injections and Imaging

All experiments were performed in accordance with the guidelines of the Animal Welfare Committee of the Royal Netherlands Academy of Arts and Sciences, The Netherlands. Tg(*TIE2:GFP*)287Sato/J mice were sedated using isoflurane inhalation anesthesia (1.5–2% isoflurane/O₂ mixture). 100 μL of DOPG liposomes (10 mM DOPG + 1% Rhod-PE) diluted 1:5 in PBS were injected retro-orbitally with an insulin syringe (BD). After 1 h, mice were sacrificed, and organs were harvested and imaged *ex vivo* on glass bottom dishes. Images were taken with a Leica SP8 multiphoton microscope with a chameleon Vision-S (Coherent Inc.), equipped with four HyD detectors: HyD1 (<455 nm), HyD2 (455–490 nm), HyD3 (500–550 nm), and HyD4 (560–650 nm). Different wavelengths between 700 nm and 1150 nm were used for excitation; HA and Rhod-PE were excited with a wavelength of 960/1050 nm and detected in HyD3 and HyD4. All images were in 12 bit and acquired with a 25× (HCX IRAPO N.A. 0.95 WD 2.5 mm) water objective.

Statistical Analysis and Data Availability

Because of small sample sizes, nonparametric tests were used exclusively. For comparisons between two groups, two-tailed Mann–Whitney tests were performed. For comparisons between multiple groups, we used Kruskal–Wallis tests followed by two-tailed Dunn’s tests with Bonferroni correction using the PMCMR package in R.⁷⁵ No statistical methods were used to predetermine sample size, but group sizes were >5 in order for the null distribution of the Kruskal–Wallis statistic to approximate the X² distribution (with *k*–1 degrees of freedom). With the exception of **Figure 1e**, graphs show all individual data points and the median. Confocal image stacks (raw data) are available from the corresponding authors upon reasonable request.

2.6 Abbreviations

CCMV VLP	cowpea chlorotic mottle virus derived virus-like particles
CHT	caudal hematopoietic tissue
CCV	common cardinal vein
CV	cardinal vein
dPCV	dorsal posterior cardinal vein
dpf	days post fertilization
DA	dorsal aorta
DLAV	dorsal longitudinal anastomotic vessel
DOPC	1,2-dioleoyl- <i>sn</i> -glycero-3-phosphocholine
DOPG	1,2-dioleoyl- <i>sn</i> -glycero-3-phospho-(1'- <i>rac</i> -glycerol)
DOPS	1,2-dioleoyl- <i>sn</i> -glycero-3-phospho-L-serine
DSPC	1,2-distearoyl- <i>sn</i> -glycero-3-phosphocholine
DOTAP	1,2-dioleoyl-3-trimethylammonium-propane
ECs	endothelial cells
fluoHA	fluorescently labeled hyaluronic acid
hpi	hour(s) post injection
ISH	<i>in situ</i> hybridization
ISV	intersegmental vessels
KCs	Kupffer cells
Li-Car	lithium carmine
LSECs	liver sinusoidal endothelial cells
MPS	mononuclear phagocyte system
OxLDL	oxidized low-density lipoprotein
PCV	posterior cardinal vein
PHS	primitive head sinus
PIB-PEG	polyisobutylene-polyethylene glycol
POPC	1-palmitoyl-2-oleoyl- <i>sn</i> -glycero-3-phosphocholine
PS-ASO	phosphothiorate-modified antisense oligonucleotides
QDs	quantum dots
RES	reticuloendothelial system
SECs	scavenging endothelial cells
vPCV	ventral posterior cardinal vein

2.7 Supporting Information

Supplementary Table 1. Nanoparticle composition, size and zeta potential. For liposomes, size and polydispersity (PDI) ranges correspond to a least three independent formulations, with the exception of:

Formulation	Composition *	Size/nm	PDI	Zeta Potential/mV
Myocet	POPC:Cholesterol (55:45)	114.5 - 122.1	0.04 - 0.06	-15.8
AmBisome	DSPC: DSPG: Cholesterol (53:21:26)	118.8 - 133.7	0.05 - 0.07	-33.7
EndoTAG-1	DOTAP:DOPC (51.5:48.5)	109.6 - 114.3	0.03 - 0.05	+46.0
Myocet (325nm)	POPC:Cholesterol (55:45)	325.4 ^a	0.22	-18.6
Myocet (465nm)	POPC:Cholesterol (55:45)	464.5 ^a	0.24	-20.0
Myocet + PEG	POPC:Cholesterol:DOPE-mPEG2000 (50:41:9)	100.4 - 118.0	0.05 - 0.06	-11.8
100% DOPC	DOPC	114.8 - 118.4	0.07 - 0.09	-11.3
100% DSPC	DSPC	102.0 - 108.3	0.06 - 0.07	-3.4
100% DOPG	DOPG	114.0 - 121.8	0.03 - 0.07	-37.1
100% DSPG	DSPG	95.4 - 102.9	0.12 - 0.17	-45.9
100% DOTAP	DOTAP	101.8 - 114.8 ^b	0.06 - 0.07	+35.6
100% POPC	POPC	108.0 - 111.4	0.07 - 0.08	-17.2
Polymersomes	PIB:PEG (1:0.75 mol ratio)	83.0	0.26	-24.0
Virus-like particles	90 CCMV capsid protein dimers	28.0	ND	-14.9 ^c
Quantum Dots	CdSe core: ZnS shell: n-octylamine-modified poly acrylic acid (PrOAm-co-PAA) copolymer cap	≈ 5 x 12 (by TEM)	ND	-70.8
Latex beads	carboxylate-modified polystyrene	121.4	0.02	-51.0

* all liposome formulations + 1 mol% DOPE-LR/+1mol% DOPE-Atto633

a. The sizes of both 'Myocet 325 nm' and 'Myocet 465 nm' liposomes varied significantly batch to batch.

b. Data for two independent formulations.

c. Zeta potential for unmodified (*i.e.* no conjugated dye) CCMV VLPs (t=3)

b. Data for two independent formulations only.

Supplementary Table 2. Liposome composition, size and encapsulated clodronic acid.

Formulation	Lipid Composition	Size/nm	PDI	Encapsulated Clodronate/ mgmL ⁻¹
100% DOPC	DOPC	126.6	0.07	0.9
100% DSPC	DSPC	128.3 - 132.2 ^a	0.06 - 0.09	1.21 - 1.72

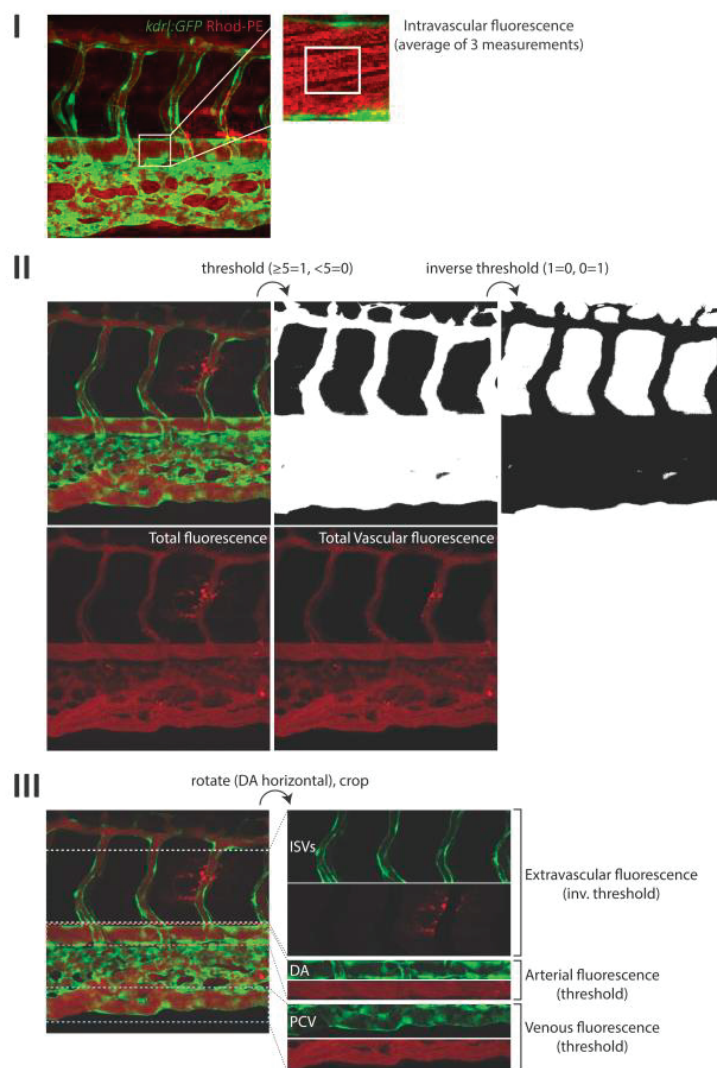
a. Data for three separate formulations

Supplementary Table 3. Guide RNA sequences and primers.

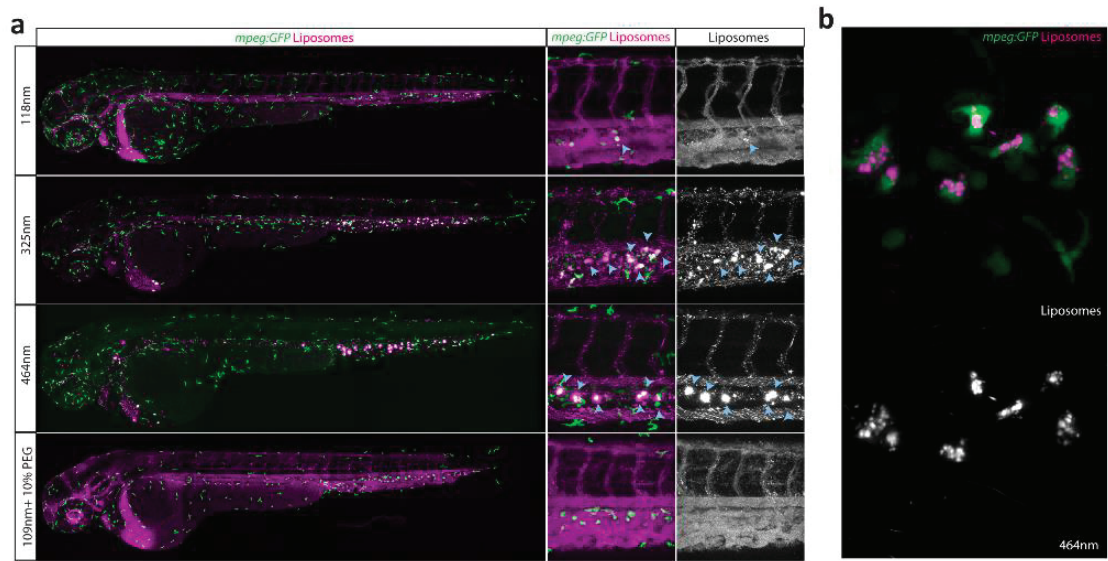
Gene	Sequences (F: Forward, R: Reverse)
Stabilin1	
sgRNA	TAATACGACTCACTATAGGATCTGATGACTCCATTCCGTTTTAGAGCTAGAAATAGC
Genotyping	F: TGTA AACGACGCGCCAGTCACCACCTGTGAACTCATAAGC R: GTGTCTTCGTTATCATT CAGGAAACAGCA
<i>In Situ</i> hybridisation	F: GAGGTTGCCATGAAGAAGCCGAC R: GCAACAACCGAAGCCAAGTCTCC
Stabilin2	
sgRNA	TAATACGACTCACTATAGGCACACACTCCTCAAGCACGTTTTAGAGCTAGAAATAGC
Genotyping	F: TGTA AACGACGCGCCAGTCCTTTTTGAACTCACAAATGCTC R: GTGTCTTGTCATACACACAGCGGGTAGAG
<i>In Situ</i> hybridisation	F: CGCCTTCGGAACATCACTATCCAG R: CCTGCAGGAGCTCAAAGACTCCAC
Mrc1a	
<i>In Situ</i> hybridisation	F: TGTGGACTGATGGTAAAGGTGTCAGC R: CTCAGGACAGTTCCTGGCATCTG

***Supplementary Figure 1. Confocal images of individual embryos that were used for image quantification.** Twelve (n=12) cellular views of Myocet, AmBisome and EndoTAG-1 liposome distribution in *kdrl*:GFP transgenic zebrafish embryos at 1,8, 24 and 48 hpi. For Myocet 48 hpi, n=11, and for EndoTAG-1 24 hpi and 48 hpi, n=6.

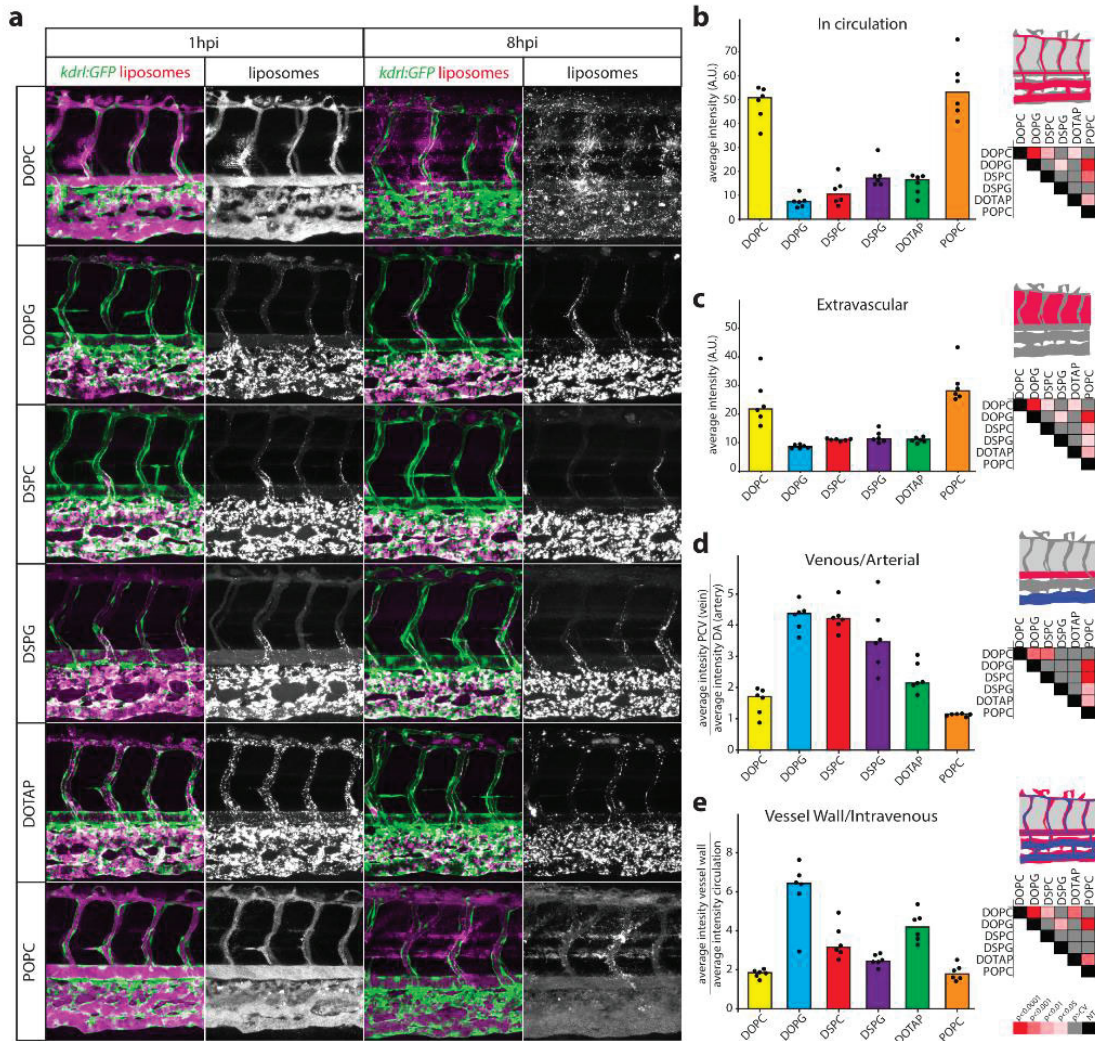
***For Supplementary Figure 1 and movies please go to:**
<https://pubs.acs.org/doi/abs/10.1021/acsnano.7b06995>.



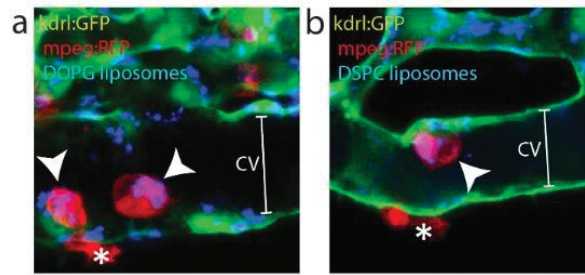
Supplementary Figure 2. Overview of quantification method as described in the Materials & Methods section. I. Quantification of intravascular fluorescence (liposomes in circulation). **II.** Quantification of total and total vascular fluorescence. **III.** Quantification of arterial, venous and extravascular fluorescence.



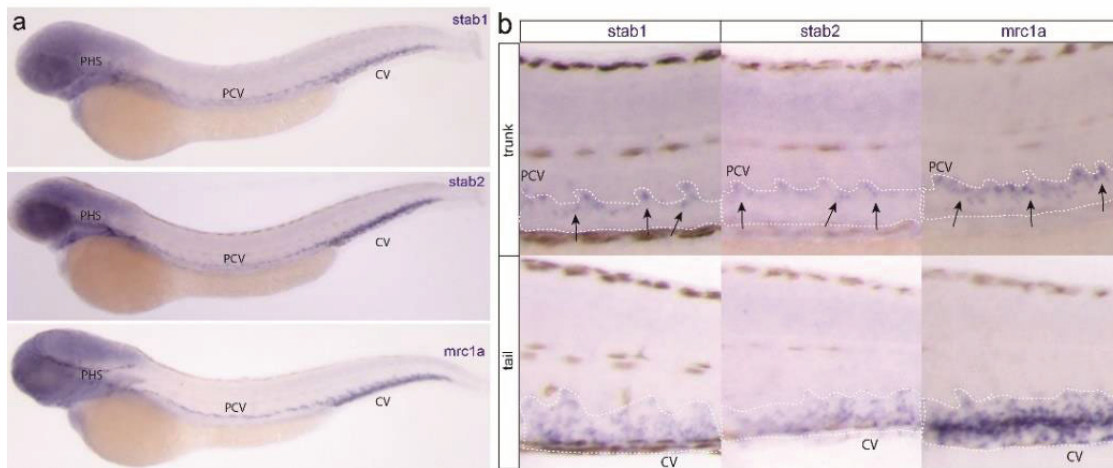
Supplementary Figure 3. Size-dependent uptake of neutral liposomes by monocytes/macrophages. (a) Whole-embryo and cellular views of liposome distribution in *mpeg1:GFP* transgenic embryos, 2h after injection with Myocet liposomes ~100 nm (with and without 10 mol% DOPE-mPEG2000), 325 nm and 464 nm pores. Immobile liposome aggregates were observed to colocalize with *mpeg1:GFP* positive macrophages/monocytes within the caudal hematopoietic tissue (CHT). Fluorescence intensity was found to increase with increased liposome size, and phagocytosis could be prevented by PEGylation. **(b)** High-resolution imaging shows intracellular localization of 400 nm liposomes within macrophages/monocytes.



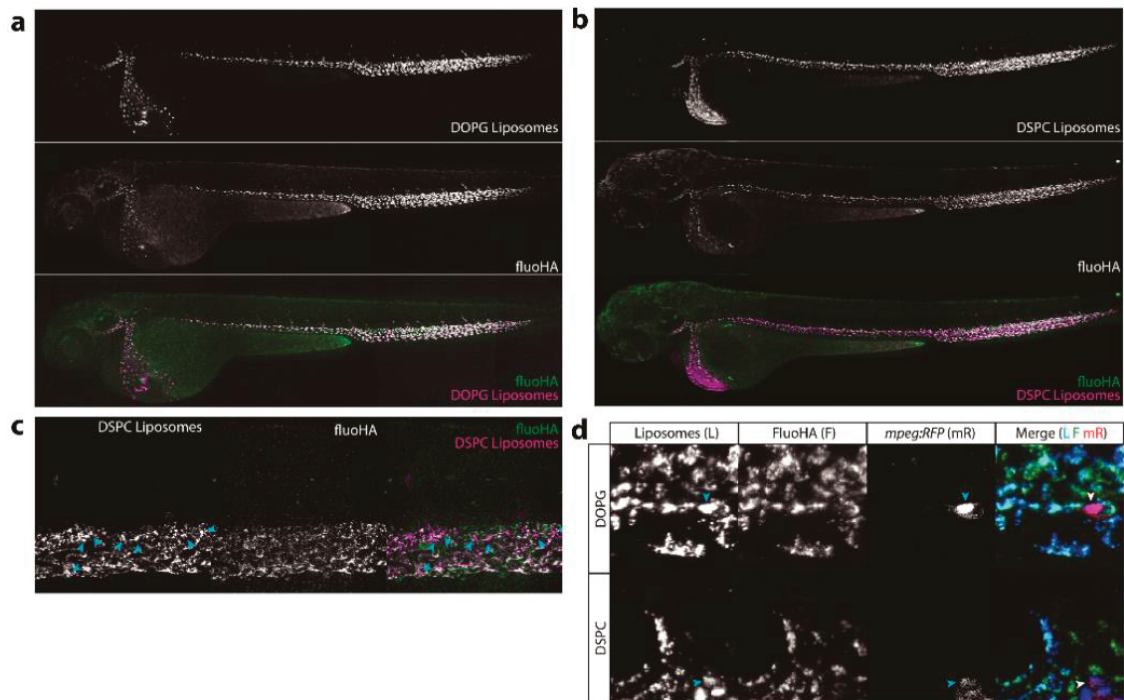
Supplementary Figure 4. Contribution of individual lipids to liposome biodistribution. (a) Cellular view of liposome distribution in *Tg(kdrl:GFP)* embryos, 1 h and 8 h after injection with liposomes generated from six different individual lipids. (b) Quantification of liposome levels in circulation based on rhodamine fluorescence intensity in the lumen of the dorsal aorta at 1 h after injection. (c) Quantification of extravascular liposome levels based on rhodamine fluorescence intensity outside of the vasculature between the DLAV and DA at 8 h after injection. (d) Quantification of liposome levels associated with venous vs. arterial endothelial cells based on rhodamine fluorescence intensity associated with caudal vein vs. DA at 8 h after injection. (e) Quantification of liposome levels associated with the vessel wall based on relative rhodamine fluorescence intensity associated with all endothelial cells vs. rhodamine fluorescence intensity in circulation at 1 h after injection. (b-e) Bar height represents median values, dots represent individual data points, significantly different pairs of values based on Kruskal-Wallis and Dunn's test with Bonferroni correction are indicated by colored boxes (representing significance levels; CV=critical value; NT=not tested). n=6 individually injected embryos per group (in 2 experiments).



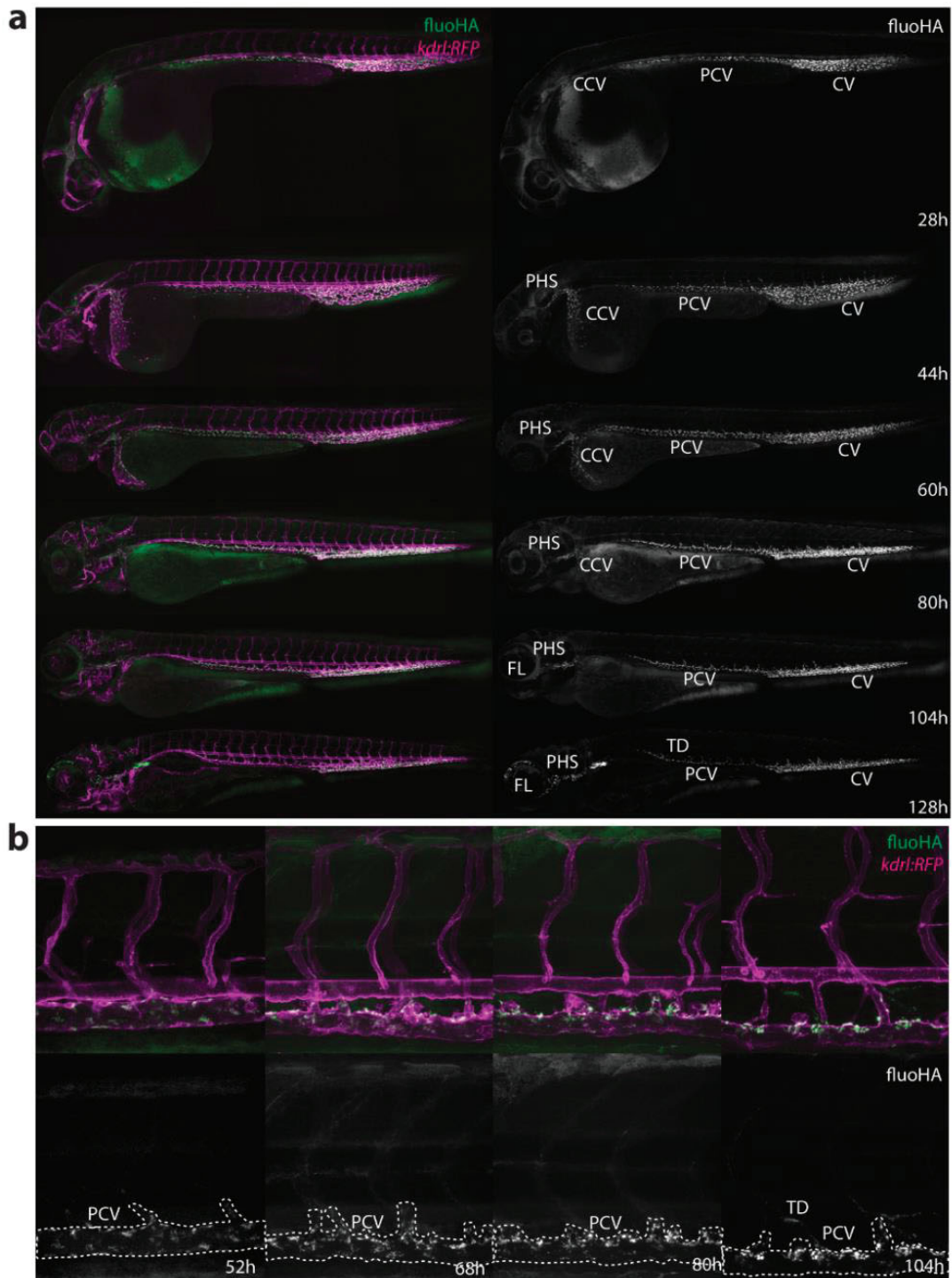
Supplementary Figure 5. Macrophage uptake of DOPG and DSPC liposomes. Confocal micrographs of *kdr1:GFP* (green); *mpeg2:RFP* (red) double transgenic embryos injected with DOPE-ATTO633 labeled DOPG **(a)** or DSPC **(b)** liposomes. Besides uptake of liposomes in caudal vein (CV, brackets) endothelial cells, uptake by plasma-exposed (arrowheads) but not extravascular (asterisks) macrophages/monocytes is also observed for both liposomes.



Supplementary Figure 6. Expression of LSEC marker genes in zebrafish embryos. **(a-b)** Whole-mount *in situ* hybridization of *stab1*, *stab2* and *mrc1a* mRNA. **(a)** Whole-embryo view showing expression of these genes in the PHS, CCV, PCV and CV **(b)** Higher-resolution image showing expression in the entire caudal vein, but only on the dorsal side of the PCV (arrows).

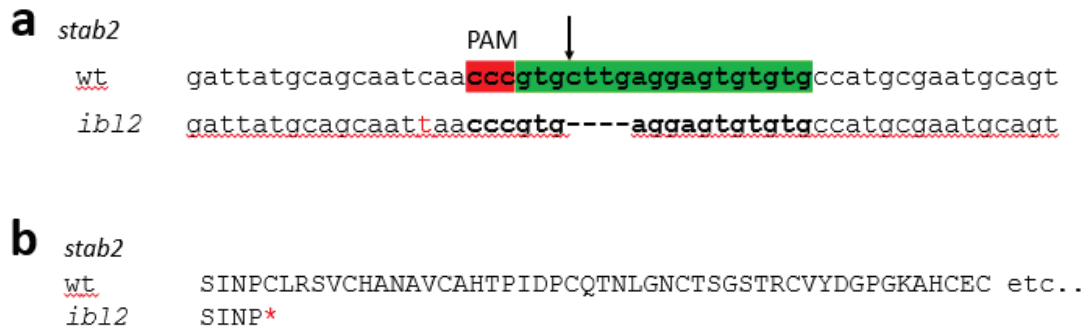


Supplementary Figure 7. Fluorimetry images showing colocalization of fluoHA with liposomes. (a-b) Whole-embryo view of co-injected fluoHA (green) and (a) DOPG liposomes or (b) DSPC liposomes (red), 1 h after injection, reveals colocalization in PHS, CCV, PCV and CV scavenger endothelial cells. (c) Tissue level view of co-injected fluoHA and DSPC liposomes, 1 h after injection reveals colocalization in SECs. Monocytes/macrophages (arrowheads) take up DSPC but not fluoHA. (d) Cellular view of co-injected fluoHA (green) and DOPG or DSPC liposomes (blue) in *mpeg:RFP* (red) transgenic embryos. Colocalization of fluoHA with both liposomes is observed in all SECs, but not in macrophages/monocytes, which only take up liposomes, but not fluoHA.

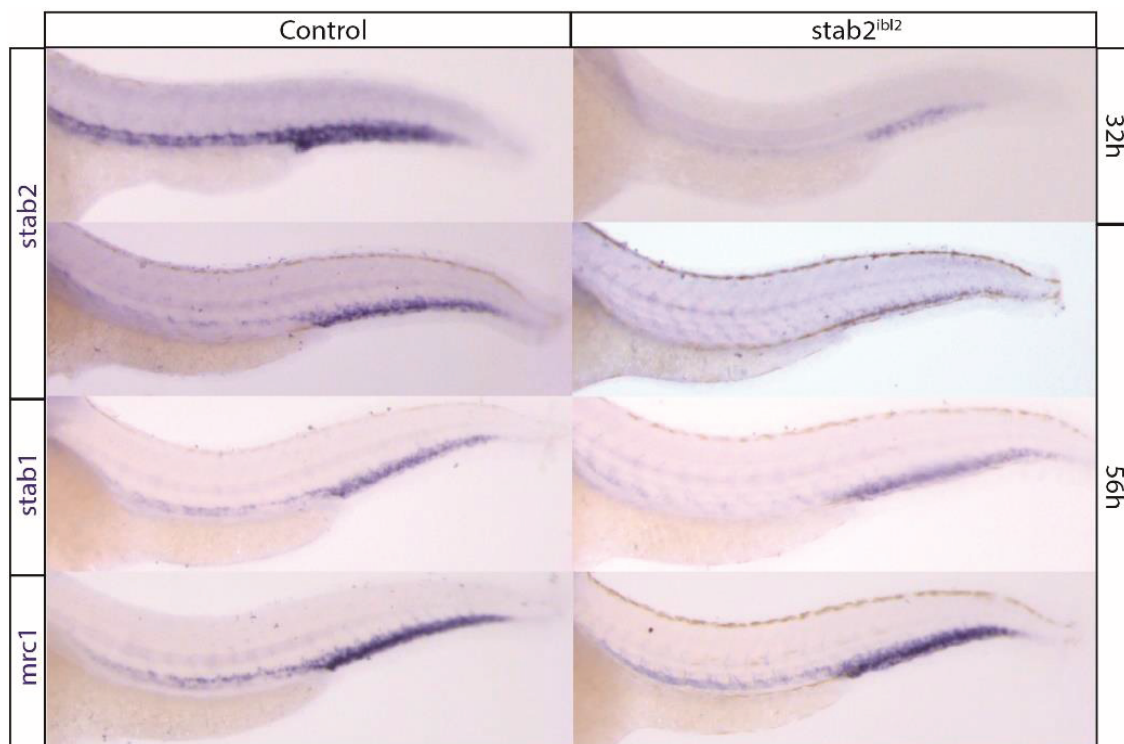


Supplementary Figure 8. FluoHA distribution through embryonic development. (a)

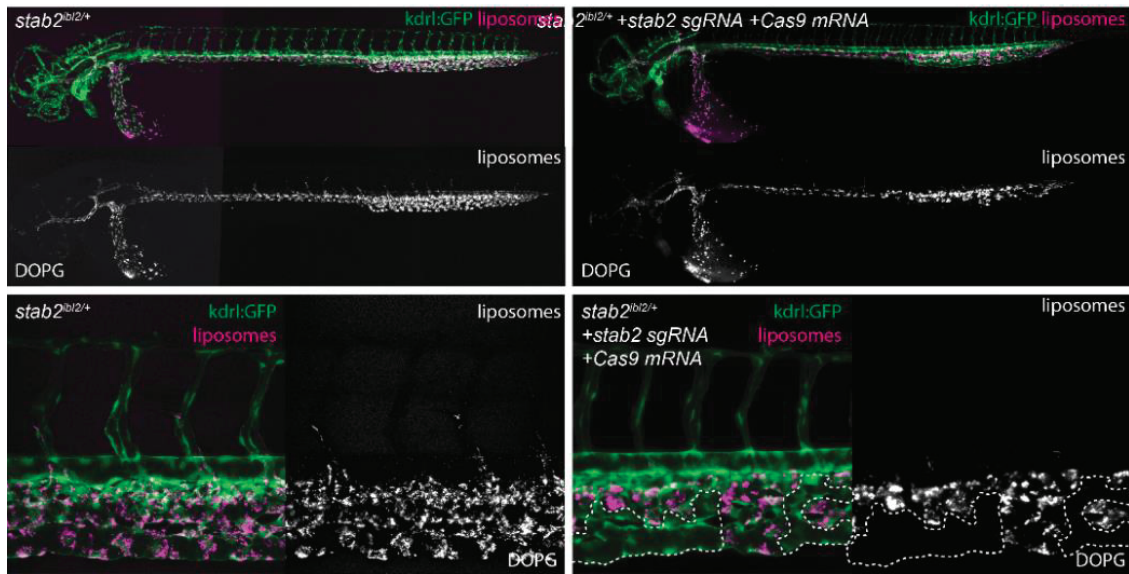
Whole-embryo view of fluorescent hyaluronic acid (fluoHA) distribution in *kdrl:RFP* transgenic embryos, 1 h after injection. SECs, as identified through intracellular accumulation of fluoHA from 28 hpf to at least 128 hpf. From 104 hpf, fluoHA uptake is also observed in lymphatic vessels, such as the thoracic duct (TD) and facial lymphatics (FL). **(b)** Cellular view of fluoHA distribution in the trunk of *kdrl:RFP* transgenic embryos, 1 h after injection. A gradual restriction of fluoHA accumulation to the PCV is observed between 52 hpf and 104 hpf.



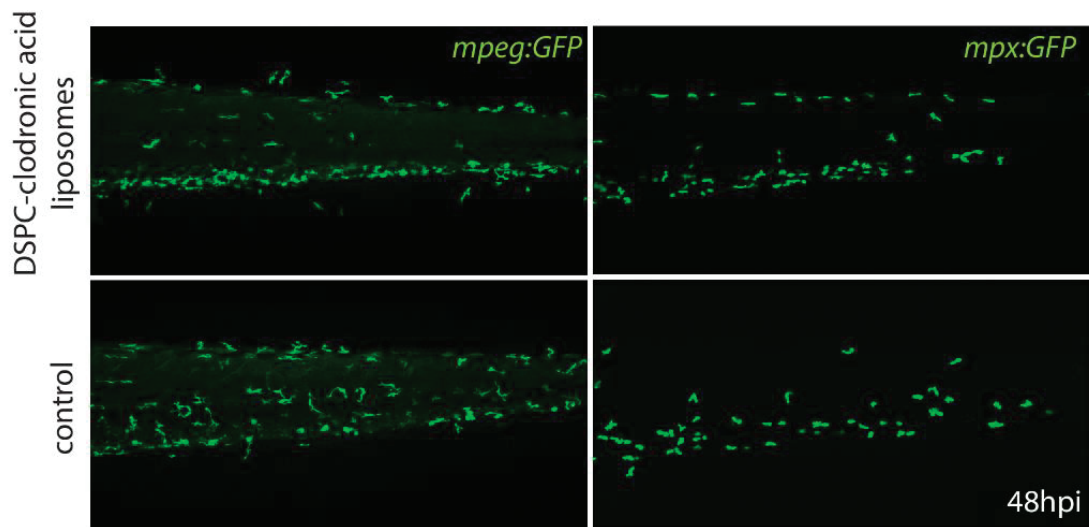
Supplementary Figure 9. CRISPR/Cas9 induced mutations. A. Nucleotide sequences surrounding the CRISPR/Cas9 targeting sites in the *stab2^{ib12}* allele. Protospacer Adjacent Motif (PAM) sequences are indicated in red, sgRNA target sites are indicated in green, arrows indicate the predicted Cas9 cutting site. A silent single-nucleotide polymorphism (C->T, red) was also identified in the *stab2^{ib12}* allele. B. Predicted amino acid sequences surrounding the CRISPR/Cas9 targeting sites in the *stab2^{ib12}* allele. Frameshift-induced amino acids and stop codons are indicated in red.



Supplementary Figure 10. Gene expression in *stab2^{ib12}* homozygous mutant embryos. Whole-mount *in situ* hybridization of *stab1* and *mrc1* mRNA expression at 56 hpf and *stab2* mRNA expression at 32 hpf and 56 hpf in the trunk and tail of *stab2^{ib12}* homozygous mutant and sibling control embryos. Reduction in *stab2* expression indicating nonsense-mediated decay of the *stab2^{ib12}* mRNA is observed *stab2^{ib12}* homozygous, but not sibling control embryos. Expression of *stab1* and *mrc1* is unchanged indicating normal SEC differentiation.



Supplementary Figure 11. Clonal *stab2* deletion. Whole-embryo and cellular views of DOPG liposome distribution in *stab2^{ib12/+}; kdr1:GFP* embryos. CRISPR/Cas9 introduced mutations in the wildtype allele generated clones of cells without *stab2* function. In *stab2* *sgRNA* and *Cas9* mRNA injected, but not control embryos, endothelial cell clones are observed in which DOPG accumulation is abrogated, indicating a requirement for *stab2* function within SECs.



Supplementary Figure 12. Cell-type selectivity of DSPC-clodronic acid liposomes. Confocal imaging of *mpeg1:GFP* (macrophage/monocytes) and *mpx:GFP* (neutrophil) transgenic zebrafish embryos 48 h after injection with 1 nl of DSPC-clodronic acid liposomes (10 mM total lipids) showing normal development of these lineages in the tail of injected embryos compared to un-injected controls (UIC).

Reagents

1,2-dioleoyl-sn-glycero-3-phosphocholine (DOPC), 1,2-distearoyl-sn-glycero-3-phosphocholine (DSPC), 1,2-dioleoyl-sn-glycero-3-phospho-(1'-rac-glycerol) (DOPG), 1,2-distearoyl-sn-glycero-3-phospho-(1'-racglycerol) (DSPG), 1-palmitoyl-2-oleoyl-sn-glycero-3-phosphocholine (POPC), 1,2-dioleoyl-sn-glycero-3-phospho-L-serine (sodium salt) (DOPS), 1,2-dioleoyl-3-trimethyl ammonium-propane (DOTAP), 1,2-dioleoyl-sn-glycero-3-phosphoethanolamine-N-[methoxy(polyethylene glycol)-2000] (DOPE-mPEG2000), 1,2-dioleoyl-sn-glycero-3-phosphoethanolamine -N-(lissamine rhodamine B sulfonyl) (Rhodamine-PE) were purchased from Avanti Polar Lipids (Alabaster, US). 1,2-Dioleoyl-sn-glycero-3-phosphoethanolamine-Atto 633 was purchased from ATTO-TEC GmbH (Germany). Additional DOPC and DSPC were purchased from Lipoid GmbH. Additional POPC and cholesterol was purchased from Sigma-Aldrich. All solvents were purchased from Biosolve Ltd. Dichloromethylenediphosphonic acid disodium salt (clodronic acid), carminic acid and dextran sulfate (40kDa) were purchased from Sigma-Aldrich. Hyaluronic acid (sodium salt, 100kDa) was purchased from Lifecore Biomedical Inc. Quantum dots (Qdot 605 ITK carboxyl) and oxidized low density lipoprotein (oxLDL from human plasma, Dil conjugate) were purchased from Thermo Fisher. 100 nm red fluorescent polystyrene, sulfate modified nanoparticles ('latex beads') were purchased from Sigma Aldrich.

Size and zeta potential measurements

Particle size and zeta potentials were measured using a Malvern Zetasizer Nano ZS. For DLS, measurements were carried out at room temperature in ddH₂O at a total lipid concentration of 100 μ M. For zeta potential measurements, liposome solutions were first diluted in salt (NaCl) solution. Zeta potentials were measured at room temperature, at 500 μ M total lipid concentration and 10 mM NaCl concentration. All reported DLS measurements and zeta potentials are the average of three measurements.

Imaging quantification

First, average intravascular fluorescence within the dorsal aorta (DA) was measured within an $\sim 8 \mu\text{m} \times 10 \mu\text{m}$ rectangular area ($\sim 1 \times 10^3$ pixels) in a single confocal slice that captured the center of the DA. This measurement was repeated three times per embryo in independent sites within the DA. Second, total fluorescence and total vasculature associated fluorescence was quantified

using the following ImageJ macro:

ImageJ quantification macro

```
rename("stack");
run("Z Project...", "projection=[Max Intensity]");
run("Split Channels");
selectWindow("C2-MAX_stack");
close();
selectWindow("C1-MAX_stack");
run("Duplicate...", "title=vascular");
selectWindow("vascular");
setThreshold(5, 255);
run("Convert to Mask");
run("Invert LUT");
run("Subtract...", "value=254");
run("Duplicate...", "title=nonvascular");
run("Macro...", "code=v=abs(v-1)");
imageCalculator("Multiply create", "vascular", "C3-MAX_stack");
imageCalculator("Multiply create", "nonvascular", "C3-MAX_stack");
selectWindow("C3-MAX_stack");
run("Measure");
selectWindow("Result of vascular");
run("Measure");
run("Concatenate...", " title=[Concatenated Stacks] keep image1=C1-MAX_stack
image2=[Result of nonvascular] image3=[Result of vascular] image4=[-- None --
]");
```

Finally, the angle of the dorsal aspect of the dorsal aorta (a straight line) was measured and the concatenated images were rotated to orient the dorsal aorta horizontally within the image. Images were subsequently cropped to a rectangle encompassing the caudal vein, DA or the area between the DA and the dorsal longitudinal anastomotic vessel (DLAV) to quantify the vasculature-associated fluorescence associated with veins (caudal vein) and arteries (DA), as well as the extravascular fluorescence around the intersegmental vessels. The latter area was used to quantify extravascular fluorescence since it does not contain pigment cells that are present on the dorsal and ventral side of the embryo and which are auto-fluorescent within the rhodamine-PE channel. Although the CHT endothelial cells appear to behave very similar to the CV endothelial cells, quantification was performed based on the CV alone for the following reasons. First, the CV is always perfused, whereas perfusion of the vessels within the CHT

is variable. Unperfused or weakly perfused vessels display absence of or reduced nanoparticle uptake. Secondly, variable numbers of hematopoietic cells - especially macrophages - are closely associated with CHT-ECs and much less with the CV. Macrophage uptake of nanoparticles could therefore lead to the false impression that CHT-ECs selectively take up nanoparticles.

From these data, the following measures were reported:

1. Average intravascular fluorescence (**Figure 1e, Supplementary Figure 4b**).
2. Venous/Arterial (**Figure 1f, 3a,b,f-k, 4a-j,m, Supplementary Figure 4d**):
(Mean CV fluorescence/%GFP positive within CV area)/(Mean DA fluorescence/%GFP positive within DA area).
3. Extravascular (**Figure 1g, Supplementary Figure 4c**): Extravascular fluorescence/%GFP negative within ISV area.
4. Vessel wall/Intravenous (**Figure 1h, Supplementary Figure 4e**): (Total vascular fluorescence/%GFP positive within the total image)/Average intravascular fluorescence.

2.8 References

1. Blanco, E.; Shen, H.; Ferrari, M., Principles of nanoparticle design for overcoming biological barriers to drug delivery. *Nat Biotechnol* **2015**, *33* (9), 941-951.
2. Dawidczyk, C. M.; Kim, C.; Park, J. H.; Russell, L. M.; Lee, K. H.; Pomper, M. G.; Searson, P. C., State-of-the-art in design rules for drug delivery platforms: lessons learned from FDA-approved nanomedicines. *J Control Release* **2014**, *187*, 133-144.
3. Wang, A. Z.; Langer, R.; Farokhzad, O. C., Nanoparticle delivery of cancer drugs. *Annu Rev Med* **2012**, *63*, 185-198.
4. Wilhelm, S.; Tavares, A. J.; Dai, Q.; Ohta, S.; Audet, J.; Dvorak, H. F.; Chan, W. C. W., Analysis of nanoparticle delivery to tumours. *Nature Reviews Materials* **2016**, *1* (5), 16014.
5. Zhang, Y. N.; Poon, W.; Tavares, A. J.; McGilvray, I. D.; Chan, W. C. W., Nanoparticle-liver interactions: Cellular uptake and hepatobiliary elimination. *J Control Release* **2016**, *240*, 332-348.
6. Bertrand, N.; Leroux, J. C., The journey of a drug-carrier in the body: an anatomo-physiological perspective. *J Control Release* **2012**, *161* (2), 152-163.
7. Kamps, J. A.; Morselt, H. W.; Swart, P. J.; Meijer, D. K.; Scherphof, G. L., Massive targeting of liposomes, surface-modified with ionized albumins, to hepatic endothelial cells. *Proc Natl Acad Sci U S A* **1997**, *94* (21), 11681-11685.
8. Park, J. K.; Utsumi, T.; Seo, Y. E.; Deng, Y.; Satoh, A.; Saltzman, W. M.; Iwakiri, Y., Cellular distribution of injected PLGA-nanoparticles in the liver. *Nanomedicine* **2016**, *12* (5), 1365-1374.
9. Tsoi, K. M.; MacParland, S. A.; Ma, X. Z.; Spetzler, V. N.; Echeverri, J.; Ouyang, B.; Fadel, S. M.; Sykes, E. A.; Goldaracena, N.; Kathis, J. M.; Conneely, J. B.; Alman, B. A.; Selzner, M.; Ostrowski, M. A.; Adeyi, O. A.; Zilman, A.; McGilvray, I. D.; Chan, W. C., Mechanism of hard-nanomaterial clearance by the liver. *Nat Mater* **2016**, *15* (11), 1212-1221.
10. Rothkopf, C.; Fahr, A.; Fricker, G.; Scherphof, G. L.; Kamps, J. A., Uptake of phosphatidylserine-containing liposomes by liver sinusoidal endothelial cells in the serum-free perfused rat liver. *Biochim Biophys Acta* **2005**, *1668* (1), 10-16.
11. Sorensen, K. K.; Simon-Santamaria, J.; McCuskey, R. S.; Smedsrod, B., Liver Sinusoidal Endothelial Cells. *Compr Physiol* **2015**, *5* (4), 1751-1774.
12. MacPhee, P. J.; Schmidt, E. E.; Groom, A. C., Intermittence of blood flow in liver sinusoids, studied by high-resolution in vivo microscopy. *Am J Physiol* **1995**, *269* (5 Pt 1), G692-698.
13. Wisse, E., An electron microscopic study of the fenestrated endothelial lining of rat liver sinusoids. *Journal of ultrastructure research* **1970**, *31* (1-2), 125-150.
14. Aschoff, L., Das reticulo-endotheliale System. In *Ergebnisse der inneren Medizin und Kinderheilkunde*, Springer: 1924; pp 1-118.
15. Seternes, T.; Sorensen, K.; Smedsrod, B., Scavenger endothelial cells of vertebrates: a nonperipheral leukocyte system for high-capacity elimination of waste macromolecules. *Proc Natl Acad Sci U S A* **2002**, *99* (11), 7594-7597.
16. Breiner, K. M.; Schaller, H.; Knolle, P. A., Endothelial cell-mediated uptake of a hepatitis B virus: a new concept of liver targeting of hepatotropic microorganisms. *Hepatology* **2001**, *34* (4 Pt 1), 803-808.
17. Ganesan, L. P.; Mohanty, S.; Kim, J.; Clark, K. R.; Robinson, J. M.; Anderson, C. L., Rapid and efficient clearance of blood-borne virus by liver sinusoidal endothelium. *PLoS Pathog* **2011**, *7* (9), e1002281.
18. Mates, J. M.; Yao, Z.; Cheplowitz, A. M.; Suer, O.; Phillips, G. S.; Kwiek, J. J.; Rajaram, M. V.; Kim, J.; Robinson, J. M.; Ganesan, L. P.; Anderson, C. L., Mouse Liver Sinusoidal Endothelium Eliminates HIV-Like Particles from Blood at a Rate of 100 Million per Minute by a Second-Order Kinetic Process. *Front Immunol* **2017**, *8*, 35.
19. Knolle, P. A.; Wohlleber, D., Immunological functions of liver sinusoidal endothelial cells. *Cell Mol Immunol* **2016**, *13* (3), 347-353.
20. Sorensen, K. K.; McCourt, P.; Berg, T.; Crossley, C.; Le Couteur, D.; Wake, K.; Smedsrod, B., The scavenger endothelial cell: a new player in homeostasis and immunity. *Am J Physiol Regul Integr Comp Physiol* **2012**, *303* (12), R1217-1230.
21. Allen, T. M.; Cullis, P. R., Liposomal drug delivery systems: from concept to clinical applications. *Adv Drug Deliv Rev* **2013**, *65* (1), 36-48.
22. Sercombe, L.; Veerati, T.; Moheimani, F.; Wu, S. Y.; Sood, A. K.; Hua, S., Advances and Challenges of Liposome Assisted Drug Delivery. *Front Pharmacol* **2015**, *6*, 286.

23. Evensen, L.; Johansen, P. L.; Koster, G.; Zhu, K.; Herfindal, L.; Speth, M.; Fenaroli, F.; Hildahl, J.; Bagherifam, S.; Tulotta, C.; Prasmickaite, L.; Maelandsmo, G. M.; Snaar-Jagalska, E.; Griffiths, G., Zebrafish as a model system for characterization of nanoparticles against cancer. *Nanoscale* **2016**, *8* (2), 862-877.
24. Fenaroli, F.; Westmoreland, D.; Benjaminsen, J.; Kolstad, T.; Skjeldal, F. M.; Meijer, A. H.; van der Vaart, M.; Ulanova, L.; Roos, N.; Nystrom, B.; Hildahl, J.; Griffiths, G., Nanoparticles as drug delivery system against tuberculosis in zebrafish embryos: direct visualization and treatment. *ACS Nano* **2014**, *8* (7), 7014-7026.
25. Jiang, X. Y.; Sarsons, C. D.; Gomez-Garcia, M. J.; Cramb, D. T.; Rinker, K. D.; Childs, S. J., Quantum dot interactions and flow effects in angiogenic zebrafish (*Danio rerio*) vessels and human endothelial cells. *Nanomedicine* **2017**, *13* (3), 999-1010.
26. Sieber, S.; Grossen, P.; Detampel, P.; Siegfried, S.; Witzigmann, D.; Huwyler, J., Zebrafish as an early stage screening tool to study the systemic circulation of nanoparticulate drug delivery systems in vivo. *J Control Release* **2017**, *264*, 180-191.
27. Batist, G.; Barton, J.; Chaikin, P.; Swenson, C.; Welles, L., Myocet (liposome-encapsulated doxorubicin citrate): a new approach in breast cancer therapy. *Expert Opin Pharmacother* **2002**, *3* (12), 1739-1751.
28. Cornely, O. A.; Maertens, J.; Bresnik, M.; Ebrahimi, R.; Ullmann, A. J.; Bouza, E.; Heussel, C. P.; Lortholary, O.; Rieger, C.; Boehme, A., et al., Liposomal amphotericin B as initial therapy for invasive mold infection: a randomized trial comparing a high-loading dose regimen with standard dosing (AmBiLoad trial). *Clin Infect Dis* **2007**, *44* (10), 1289-1297.
29. Schmitt-Sody, M.; Strieth, S.; Krasnici, S.; Sauer, B.; Schulze, B.; Teifel, M.; Michaelis, U.; Naujoks, K.; Dellian, M., Neovascular targeting therapy: paclitaxel encapsulated in cationic liposomes improves antitumoral efficacy. *Clin Cancer Res* **2003**, *9* (6), 2335-2341.
30. Immordino, M. L.; Dosio, F.; Cattel, L., Stealth liposomes: review of the basic science, rationale, and clinical applications, existing and potential. *Int J Nanomedicine* **2006**, *1* (3), 297-315.
31. Murayama, E.; Kissa, K.; Zapata, A.; Mordelet, E.; Briolat, V.; Lin, H. F.; Handin, R. I.; Herbomel, P., Tracing hematopoietic precursor migration to successive hematopoietic organs during zebrafish development. *Immunity* **2006**, *25* (6), 963-975.
32. Isogai, S.; Horiguchi, M.; Weinstein, B. M., The vascular anatomy of the developing zebrafish: an atlas of embryonic and early larval development. *Dev Biol* **2001**, *230* (2), 278-301.
33. Cho, E. C.; Xie, J.; Wurm, P. A.; Xia, Y., Understanding the role of surface charges in cellular adsorption versus internalization by selectively removing gold nanoparticles on the cell surface with a I2/KI etchant. *Nano Lett* **2009**, *9* (3), 1080-1084.
34. Hen, G.; Nicenboim, J.; Maysel, O.; Asaf, L.; Shin, M.; Busolin, G.; Hofi, R.; Almog, G.; Tiso, N.; Lawson, N. D.; Yaniv, K., Venous-derived angioblasts generate organ-specific vessels during zebrafish embryonic development. *Development* **2015**, *142* (24), 4266-4278.
35. Koltowska, K.; Paterson, S.; Bower, N. I.; Baillie, G. J.; Legendijk, A. K.; Astin, J. W.; Chen, H.; Francois, M.; Crosier, P. S.; Taft, R. J.; Simons, C.; Smith, K. A.; Hogan, B. M., *mafba* is a downstream transcriptional effector of Vegfc signaling essential for embryonic lymphangiogenesis in zebrafish. *Genes Dev* **2015**, *29* (15), 1618-1630.
36. Stapelfeldt, H.; Jun, H.; Skibsted, L. H., Fluorescence properties of carminic acid in relation to aggregation, complex formation and oxygen activation in aqueous food models. *Food chemistry* **1993**, *48* (1), 1-11.
37. Schledzewski, K.; Geraud, C.; Arnold, B.; Wang, S.; Grone, H. J.; Kempf, T.; Wollert, K. C.; Straub, B. K.; Schirmacher, P.; Demory, A.; Schonhaber, H.; Gratchev, A.; Dietz, L.; Thierse, H. J.; Kzhyshkowska, J.; Goerdts, S., Deficiency of liver sinusoidal scavenger receptors stabilin-1 and -2 in mice causes glomerulofibrotic nephropathy via impaired hepatic clearance of noxious blood factors. *J Clin Invest* **2011**, *121* (2), 703-714.
38. Hogan, B. M.; Bos, F. L.; Bussmann, J.; Witte, M.; Chi, N. C.; Duckers, H. J.; Schulte-Merker, S., *Ccbe1* is required for embryonic lymphangiogenesis and venous sprouting. *Nat Genet* **2009**, *41* (4), 396-398.
39. Wong, K. S.; Proulx, K.; Rost, M. S.; Sumanas, S., Identification of vasculature-specific genes by microarray analysis of *Etsrp/Etv2* overexpressing zebrafish embryos. *Dev Dyn* **2009**, *238* (7), 1836-1850.
40. Zhou, B.; Weigel, J. A.; Fauss, L.; Weigel, P. H., Identification of the hyaluronan receptor for endocytosis (HARE). *J Biol Chem* **2000**, *275* (48), 37733-37741.

41. Simon-Santamaria, J.; Malovic, I.; Warren, A.; Oteiza, A.; Le Couteur, D.; Smedsrod, B.; McCourt, P.; Sorensen, K. K., Age-related changes in scavenger receptor-mediated endocytosis in rat liver sinusoidal endothelial cells. *J Gerontol A Biol Sci Med Sci* **2010**, *65* (9), 951-960.
42. Miller, C. M.; Donner, A. J.; Blank, E. E.; Egger, A. W.; Kellar, B. M.; Ostergaard, M. E.; Seth, P. P.; Harris, E. N., Stabilin-1 and Stabilin-2 are specific receptors for the cellular internalization of phosphorothioate-modified antisense oligonucleotides (ASOs) in the liver. *Nucleic Acids Res* **2016**, *44* (6), 2782-2794.
43. Park, S. Y.; Jung, M. Y.; Kim, H. J.; Lee, S. J.; Kim, S. Y.; Lee, B. H.; Kwon, T. H.; Park, R. W.; Kim, I. S., Rapid cell corpse clearance by stabilin-2, a membrane phosphatidylserine receptor. *Cell Death Differ* **2008**, *15* (1), 192-201.
44. Balogh, P.; Petz, A., Selective binding of biotinylated albumin to the lymphoid microvasculature. *Histochem Cell Biol* **2005**, *123* (4-5), 357-363.
45. Alidori, S.; Bowman, R. L.; Yarilin, D.; Romin, Y.; Barlas, A.; Mulvey, J. J.; Fujisawa, S.; Xu, K.; Ruggiero, A.; Riabov, V.; Thorek, D. L.; Ulmert, H. D.; Brea, E. J.; Behling, K.; Kzhyshkowska, J.; Manova-Todorova, K.; Scheinberg, D. A.; McDevitt, M. R., Deconvoluting hepatic processing of carbon nanotubes. *Nat Commun* **2016**, *7*, 12343.
46. Lee, S. J.; Park, S. Y.; Jung, M. Y.; Bae, S. M.; Kim, I. S., Mechanism for phosphatidylserine-dependent erythrophagocytosis in mouse liver. *Blood* **2011**, *117* (19), 5215-5223.
47. Harris, E. N.; Weigel, P. H., The ligand-binding profile of HARE: hyaluronan and chondroitin sulfates A, C, and D bind to overlapping sites distinct from the sites for heparin, acetylated low-density lipoprotein, dermatan sulfate, and CS-E. *Glycobiology* **2008**, *18* (8), 638-648.
48. Tamura, Y.; Adachi, H.; Osuga, J.; Ohashi, K.; Yahagi, N.; Sekiya, M.; Okazaki, H.; Tomita, S.; Iizuka, Y.; Shimano, H.; Nagai, R.; Kimura, S.; Tsujimoto, M.; Ishibashi, S., FEEL-1 and FEEL-2 are endocytic receptors for advanced glycation end products. *J Biol Chem* **2003**, *278* (15), 12613-12617.
49. Kawasaki, T.; Etoh, R.; Yamashina, I., Isolation and characterization of a mannan-binding protein from rabbit liver. *Biochem Biophys Res Commun* **1978**, *81* (3), 1018-1024.
50. Rost, M. S.; Sumanas, S., Hyaluronic acid receptor Stabilin-2 regulates Erk phosphorylation and arterial-venous differentiation in zebrafish. *PLoS One* **2014**, *9* (2), e88614.
51. Stoll, S. J.; Bartsch, S.; Kroll, J., HOXC9 regulates formation of parachordal lymphangioplasts and the thoracic duct in zebrafish via stabilin 2. *PLoS One* **2013**, *8* (3), e58311.
52. Hirose, Y.; Saijou, E.; Sugano, Y.; Takeshita, F.; Nishimura, S.; Nonaka, H.; Chen, Y. R.; Sekine, K.; Kido, T.; Nakamura, T.; Kato, S.; Kanke, T.; Nakamura, K.; Nagai, R.; Ochiya, T.; Miyajima, A., Inhibition of Stabilin-2 elevates circulating hyaluronic acid levels and prevents tumor metastasis. *Proc Natl Acad Sci U S A* **2012**, *109* (11), 4263-4268.
53. Verwegen, M.; Cornelissen, J. J., Clustered nanocarriers: the effect of size on the clustering of CCMV virus-like particles with soft macromolecules. *Macromol Biosci* **2015**, *15* (1), 98-110.
54. Askes, S. H.; Pomp, W.; Hopkins, S. L.; Kros, A.; Wu, S.; Schmidt, T.; Bonnet, S., Imaging Upconverting Polymersomes in Cancer Cells: Biocompatible Antioxidants Brighten Triplet-Triplet Annihilation Upconversion. *Small* **2016**, *12* (40), 5579-5590.
55. Plosker, G. L.; Goa, K. L., Clodronate. A review of its pharmacological properties and therapeutic efficacy in resorptive bone disease. *Drugs* **1994**, *47* (6), 945-982.
56. van Rooijen, N.; Hendriks, E., Liposomes for specific depletion of macrophages from organs and tissues. *Methods Mol Biol* **2010**, *605*, 189-203.
57. Michen, B.; Graule, T., Isoelectric points of viruses. *J Appl Microbiol* **2010**, *109* (2), 388-397.
58. Elvevold, K.; Smedsrod, B.; Martinez, I., The liver sinusoidal endothelial cell: a cell type of controversial and confusing identity. *Am J Physiol Gastrointest Liver Physiol* **2008**, *294* (2), G391-400.
59. Patel, K. R.; Li, M. P.; Baldeschwieler, J. D., Suppression of liver uptake of liposomes by dextran sulfate 500. *Proc Natl Acad Sci U S A* **1983**, *80* (21), 6518-6522.
60. de Belder, A. N.; Wik, K. O., Preparation and properties of fluorescein-labelled hyaluronate. *Carbohydr Res* **1975**, *44* (2), 251-257.
61. Kawai, Y.; Smedsrod, B.; Elvevold, K.; Wake, K., Uptake of lithium carmine by sinusoidal endothelial and Kupffer cells of the rat liver: new insights into the classical vital staining and the reticulo-endothelial system. *Cell Tissue Res* **1998**, *292* (2), 395-410.
62. Voloshin, T.; Alishekevitz, D.; Kaneti, L.; Miller, V.; Isakov, E.; Kaplanov, I.; Voronov, E.; Fremder, E.; Benhar, M.; Machluf, M.; Apte, R. N.; Shaked, Y., Blocking IL1beta Pathway Following Paclitaxel Chemotherapy Slightly Inhibits Primary Tumor Growth but Promotes Spontaneous Metastasis. *Mol Cancer Ther* **2015**, *14* (6), 1385-1394.

63. Jin, S. W.; Beis, D.; Mitchell, T.; Chen, J. N.; Stainier, D. Y., Cellular and molecular analyses of vascular tube and lumen formation in zebrafish. *Development* **2005**, *132* (23), 5199-5209.
64. Ellett, F.; Pase, L.; Hayman, J. W.; Andrianopoulos, A.; Lieschke, G. J., mpeg1 promoter transgenes direct macrophage-lineage expression in zebrafish. *Blood* **2011**, *117* (4), e49-56.
65. Nguyen-Chi, M.; Phan, Q. T.; Gonzalez, C.; Dubremetz, J. F.; Levraud, J. P.; Lutfalla, G., Transient infection of the zebrafish notochord with E. coli induces chronic inflammation. *Dis Model Mech* **2014**, *7* (7), 871-882.
66. Bussmann, J.; Bos, F. L.; Urasaki, A.; Kawakami, K.; Duckers, H. J.; Schulte-Merker, S., Arteries provide essential guidance cues for lymphatic endothelial cells in the zebrafish trunk. *Development* **2010**, *137* (16), 2653-2657.
67. Hogan, B. M.; Herpers, R.; Witte, M.; Helotera, H.; Alitalo, K.; Duckers, H. J.; Schulte-Merker, S., Vegfc/Flt4 signalling is suppressed by Dll4 in developing zebrafish intersegmental arteries. *Development* **2009**, *136* (23), 4001-4009.
68. Mathias, J. R.; Perrin, B. J.; Liu, T. X.; Kanki, J.; Look, A. T.; Huttenlocher, A., Resolution of inflammation by retrograde chemotaxis of neutrophils in transgenic zebrafish. *J Leukoc Biol* **2006**, *80* (6), 1281-1288.
69. Thisse, C.; Thisse, B., High-resolution in situ hybridization to whole-mount zebrafish embryos. *Nat Protoc* **2008**, *3* (1), 59-69.
70. Varshney, G. K.; Pei, W.; LaFave, M. C.; Idol, J.; Xu, L.; Gallardo, V.; Carrington, B.; Bishop, K.; Jones, M.; Li, M.; Harper, U.; Huang, S. C.; Prakash, A.; Chen, W.; Sood, R.; Ledin, J.; Burgess, S. M., High-throughput gene targeting and phenotyping in zebrafish using CRISPR/Cas9. *Genome Res* **2015**, *25* (7), 1030-1042.
71. Carrington, B.; Varshney, G. K.; Burgess, S. M.; Sood, R., CRISPR-STAT: an easy and reliable PCR-based method to evaluate target-specific sgRNA activity. *Nucleic Acids Res* **2015**, *43* (22), e157.
72. Weinstein, B. M.; Stemple, D. L.; Driever, W.; Fishman, M. C., Gridlock, a localized heritable vascular patterning defect in the zebrafish. *Nat Med* **1995**, *1* (11), 1143-1147.
73. Schindelin, J.; Arganda-Carreras, I.; Frise, E.; Kaynig, V.; Longair, M.; Pietzsch, T.; Preibisch, S.; Rueden, C.; Saalfeld, S.; Schmid, B.; Tinevez, J. Y.; White, D. J.; Hartenstein, V.; Eliceiri, K.; Tomancak, P.; Cardona, A., Fiji: an open-source platform for biological-image analysis. *Nat Methods* **2012**, *9* (7), 676-682.
74. Schneider, C. A.; Rasband, W. S.; Eliceiri, K. W., NIH Image to ImageJ: 25 years of image analysis. *Nat Methods* **2012**, *9* (7), 671-675.
75. Pohlert, T., The pairwise multiple comparison of mean ranks package (PMCMR). *R package* **2014**, *27* (2020), 10.

